AN ENHANCEMENT OF LIGHT REFLECTANCE SPECTROSCOPY AS A MODALITY FOR THE DETECTION OF POSITIVE SURGICAL MARGINS IN RADICAL PROSTATECTOMY

By

Zengxing Pang

A THESIS SUBMITTED IN PARTIAL FULFILLMENT OF THE REQUIREMENTS FOR

THE MASTER'S DEGREE

OF SCIENCE IN

BIOMEDICAL ENGINEERING

UNIVERSITY OF TEXAS AT ARLINGTON

AUGUST 2018

ACKNOWLEDGEMENTS

As I am beginning to gather and write down my thoughts for this thesis' introductory segment, I feel a sense of relief that arises from having arrived to the concluding steps of this project, but more powerfully, I feel myself being filled with tremendous gratitude for all of the people who magnanimously lent me their guidance and helping hands as I moved from one obstacle to the next during the course of this research. As Issac Newton once keenly said, "If I have seen a little further, it is by standing on the shoulders of giants." Nevermore had this quote become more relevant as I took a deeper dive into the world of engineering and scientific research in the past year. In fact, I often found myself directly experiencing this wise analogy of "standing on giants' shoulders" as I consulted with numerous mentors and peers at different major turning points of my work. As such, if I have made any contribution to the ongoing progress of prostate cancer research, I could not have done so without the kind of assistance described by Newton. Without further ado, I would like to individually honor and express my deep gratitude for all of the generous giants who chose to lend me their blessings.

First and foremost, I must thank my Mentor, Dr. Hanli Liu, who allowed me the priceless opportunity to conduct research and to compile this work of thesis under her supervision. Among all students, domestic or international, who study in the department of Bioengineering at this university, I consider myself a truly lucky student who has had the fortune of working under such a supportive, knowledgeable, and dedicated professor. Throughout the course of this research, she had given me just the right

amount of freedom to explore my own creativity, all the while never forgetting to offer constructive criticism every time she saw that my ideas and directions were in need of a reality check. As a mentor, Dr. Liu has instilled in me a stronger sense of professionalism, responsibility, decisiveness, and scholarly diplomacy. I had always struggled with being overly perfectionist, and would often sacrifice unrealistic amounts of time over small details that did not deserve such scrutiny. Without Dr. Liu's decisive instructions and insightful feedbacks, I would have failed to meet many deadlines, let alone having finished this thesis in a timely manner. Dr. Liu has also taught me the invaluable lesson of effective communications, as there were a number of occasions where she and I wound up on different pages simply due to my not keeping our line of communication open whilst exploring certain design ideas. From these experiences, I have awakened to the crucial nature of clear and frequent communications in a collaborative research or engineering environment. It is said that no man is an island, and Dr. Liu has helped me to see that any man who attempts to be his own island in science and engineering could only delay his and everyone else's progress. In addition to everything above, Dr. Liu also demonstrated her exemplary social skills in formal communication; in this project, we often had to consult with engineers from our sister research institute, UTARI, and occasionally with the clinicians at UTSW; and Dr. Liu's professional conducts had always allowed meetings with our collaborators to be fruitful with clearer objectives and resolved issues. For all of the valuable lessons from Dr. Liu, I remain always grateful for her being such a cultivating mentor, and I will carry on her teachings into my own practice as I venture onward in my career.

Next, I would like to pay tribute to both groups of collaborators whose efforts significantly accelerated the progress of this thesis project. I owe many thanks to Dr. Jeffery Cadeddu, the distinguished clinician from UTSW who funded this research. He and Dr. Liu had been collaborating for nearly ten years on various prostate cancer imaging projects, and I am much honored to be taken on board and to add further contributions to their cause. Another influential collaborator is Dr. Aditya Das, the division head of automation and intelligent systems department from the much esteemed university research institute (UTARI), who made major contributions to this project with his extensive technical and software understanding. Without the frequent help and suggestions from him and his talented research engineer Michael Araujo, both the physical handheld prototype device, along with its customized graphical interface in LabVIEW, would not have advanced to the current operating status. Due to my limited understanding of both 3-D drafting and signal processing via a data acquisition module, I had to make many trips to UTARI to consult with both Dr. Das and Michael, both of whom have been very generous and willing to share their expertise, despite me often having to cut into the time they needed for other projects at hand.

On top of all the greatly supportive figures mentioned above, I am additionally lucky to have been guided by many mentors from the Bioengineering department itself. Many thanks to Xinglong Wang, Ph.D, the post-doctorate researcher in our lab, for he oversaw much of this project in its entire duration. There was no one so experienced and sharing such as Xinglong, with whom I could discuss my experimental methods in detail. Every time I had confusion over my experiments, the only person who would offer

his immediate suggestions was Xinglong; I was often amazed by how much knowledge and understanding he had gathered in his academic career, as he was able to offer useful perspectives every time I sought his help. I admire Xinlong for having been such a good role model as a more experienced academic, and most of all, his openness to always help the less experienced students like me. Henry Chan is another mentor whom I have a lot to thank for. Although Henry was a colleague who attended many of the same graduate level courses as I did, he had year of former experience on this research, and thus he was senior of me. It was he who initially referred me to Dr. Liu to work in her lab, and shortly after I had joined the lab, it was also Henry who took the extra time to bring me up to speed with the inner-workings of this research; I am extremely thankful to him for introducing me to this work. Furthermore, I would like to acknowledge and thank Dr. Chuong, for pointing me to the right direction as I ventured through the fascinating courses within the bioengineering curriculum. Further thanks to Ms. Rockrow for being such an incredibly compassionate advisor, who always go above and beyond to ensure that her students are in good academic standing.

Last but not the least, I would like to express my most immense gratitude towards my mother and stepfather. Throughout the many years we have shared together, never once did they cease to provide the utmost understanding, tolerance, discipline, and support. Not only have they shown me unconditional love, but most importantly, they have through their own conducts, defined what it means to be a kind and upright human being. For all of their gifts that I cannot return in exact value, I can only redeem myself in hopes that my actions and achievements will make them more and more proud

throughout this life. Finally, I am much obliged to voice my deep appreciation for my partner, Laura, whose loving companionship have enriched the colors of my life unlike anyone has ever done before.

Zengxing Pang,

07.08.2018.

Abstract

AN ENHANCEMENT OF LIGHT REFLECTANCE SPECTROSCOPY AS A MODALITY FOR THE DETECTION OF POSITIVE SURGICAL MARGINS IN PROSTATECTOMY,

Zengxing Pang, MS

University of Texas at Arlington, 2018

Light Reflectance Spectroscopy (LRS) is an imaging method that has shown increasingly promising evidence in its ability to detect various forms of cancer tissues. Our previous studies have illustrated the LRS modality's capacity to differentiate normal and cancerous prostate tissues, specifically in its effectiveness in distinguishing cancer tissues classified 4+3 and 4+4 in Gleason Score. Despite having shown sufficient sensitivity and specificity towards prostate cancer detection, the pre-existing imaging system remains impractical for its intended clinical application of detecting positive surgical margins during prostatectomy. Two of the biggest challenges in the current equipment include lack of mobility and slow data collection, which stifles LRS's advantage of being able to stream data in real time. This is largely due to the LRS fiber optic needle being fixed by a stationary clamp and being covered by a bulky black box as shielding from spectral noise from the environment. In this study, a novel handheld device was researched and developed to overcome the inconveniencing aspects of the LRS equipment, where the needle probe was placed into a 3D printed casing and utilized in a stylus fashion. This removed the need for the aforementioned stage and box shielding, which greatly enhanced the system's mobility. Furthermore, a tactile switch was incorporated into the 3D printed device so that data could be streamed and collected without direct interaction with computer software, thus further increasing the

user-friendliness of the modality. The effectiveness of this new approach was tested against the traditional set-up, and as a result, it was discovered that the newly developed device functions optimally in low light conditions. In addition, it was discovered that the enhanced system, due to being purely handheld, contains a higher magnitude of human error that results from inconsistently applied pressure. Therefore, further studies will be required to improve the consistency new LRS device before it can be transferred into direct clinical usage.

Table of Contents

Chapter 1: Introduction

1.1 The Human Prostate:

The prostate is a gland organ that encapsulates the urethra and is only found in males. On average, it is approximately 3 x 4 x 2 cm in dimension and 20 grams in mass[2]. Located anterior to the rectum and inferior to bladder, the prostate is primarily understood to facilitate sperm motility via the joint production of seminal fluid with the cooperation of seminal vesicles, which connects into the prostate[2].

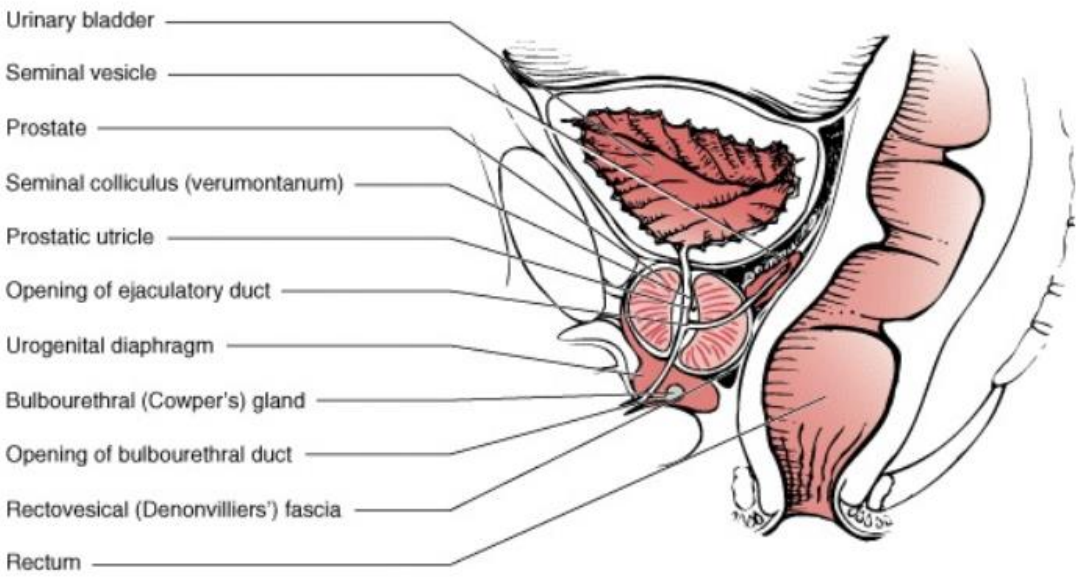

Figure 1. The human anatomy surrounding the human prostate[1]

Structurally, the human prostate is separated into four major zones: Anterior fibromuscular, Peripheral, Central, and Transitional. While the Anterior fibromuscular zone accounts for 30% of the prostate's overall mass, it does not include any glandular

elements and is mainly composed of smooth muscle cells, however, the remaining zones all contain glandular epithelial elements, with the peripheral zone having the most amount, comprising nearly 75% of the total glandular elements found throughout the prostate; due to this, the peripheral zone is the site where of most prostatic carcinomas are found[1,2].

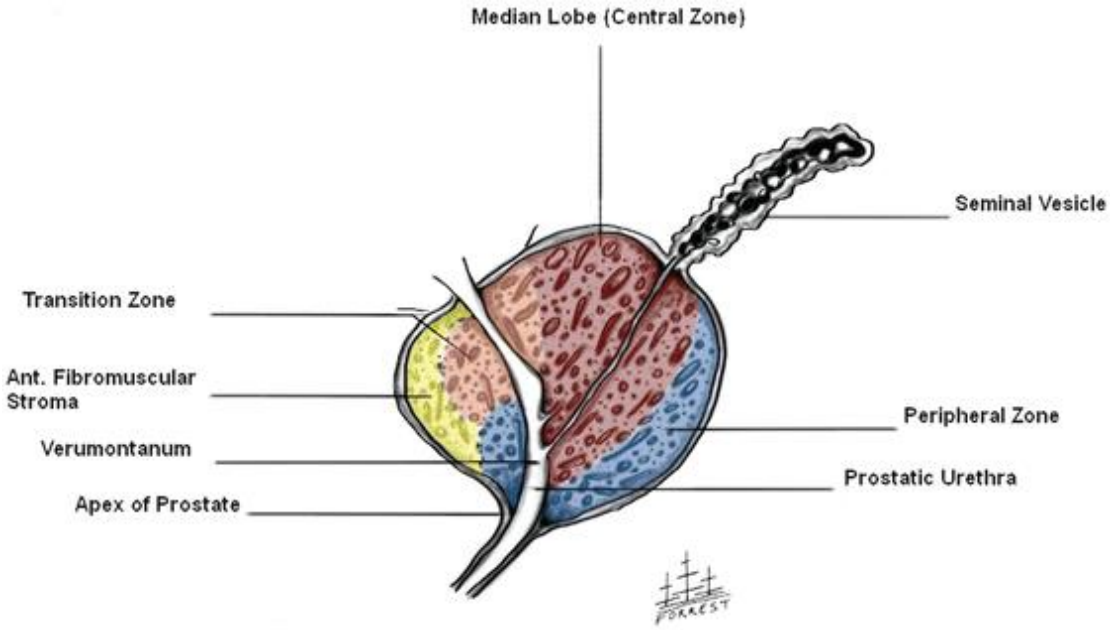

Figure 2. Various defined Zones of the Prostate[2].

The central zone contains the remaining majority of the glandular elements, and is the area surrounding the ejaculation ducts. The last major area of the prostate is the transition zone, which sits between the anterior fibromuscular and central zones; it has a small amount of glands, not exceeding 5% of the entire prostate. Despite this, the transitional zone accounts between 15 to 30% of the prostate volume, and is the site where benign prostatic hyperplasia (BPH) occurs. Not to be mistaken as prostate cancer, BPH is a condition in which the prostate undergoes enlargement, which can result in urinary obstruction and irritations[2,3].

1.2 Prostate Cancer: Introduction

From the late twentieth century to the present day, prostate cancer has become increasingly common, to the point where it is now the most frequently diagnosed form of cancer among US men, apart from nonmelanoma skin cancer[4]. By 2015, there were approximately 1,600,000 diagnosed cases worldwide[5]. And within the US, nearly 192,000 individuals are diagnosed with prostate cancer every year[6]. Moreover, although prostate cancer is conventionally diagnosed in men who are 55 years or older, during the past two decades, evidence has shown that the incidence rate of this type of cancer has noticeably increased for men aged 55 years or younger. From 1986 to 2008, while the incidence rate across all ages had raised from 113 to 163 cases per 100,000 person years, that of the younger men's population (55 years or younger) had jumped from 5.6 to 32 cases, which is nearly a 6-fold increase. This alarmingly disproportional surge of prostate cancer rate in younger men further stresses the present-day importance in the ongoing research and investigation of this growing disease[7].

The exact causes of prostate cancer cannot be pinpointed with the present-day medical knowledge, nonetheless, much of the current epidemiological studies highlight nutrition and lifestyle having significant associations with the progression and the risk of prostate cancer. In terms of lifestyle, high body mass indexes (BMIs) and smoking have the highest strength of evidence linked to the progression of prostate cancer, where both activities are associated with higher prostate cancer-specific mortality[4,8]. For instance, in a meta-analysis of clinical statistics, it was revealed that a 5 kg/m^2 increase of BMI

elevated the risk of prostate cancer-specific mortality by 20% and biochemical recurrence (resurged levels of prostate-specific antigen after treatment) by 21% compared to men with healthy BMI readings[9]. Further, smoking is known to show longer lasting effects with respect to prostate cancer, with studies suggesting significantly increased mortality and biochemical recurrence rates, as much as 60%, for prostate cancer subjects who report to smoke regularly[10]. With regard to nutrition, excessive intake of diary-based products, total and saturated fat, as well as refined carbohydrates have all known to promote prostate cancer progression[8,11]. To avert risk of developing prostate cancer via nutrition and life style, numerous contemporary studies recommend regular physical activity to maintain healthy body weights, including more portions of antioxidant rich fruits and vegetables, and replacing saturated fats found in animal meat and corn oil with omega-3 fats, which are commonly found in fish oil[4,8,12].

1.3 Prostate Cancer: Classification and The Gleason Grading

Prostate cancer survival is highly correlated to the pathological Gleason grades, a long-established grading system that is the current standard for defining the severity of prostate cancer via histological samples collected in prostate biopsies, where a handheld needle gun is inserted into the rectum to collect prostate tissue in the amount typically 10 to 20 needle cores[13,14]. The figure below illustrates the morphology of each grade. The gland structures become increasingly fused as the grade level increases, and so does the severity of the prostate cancer.

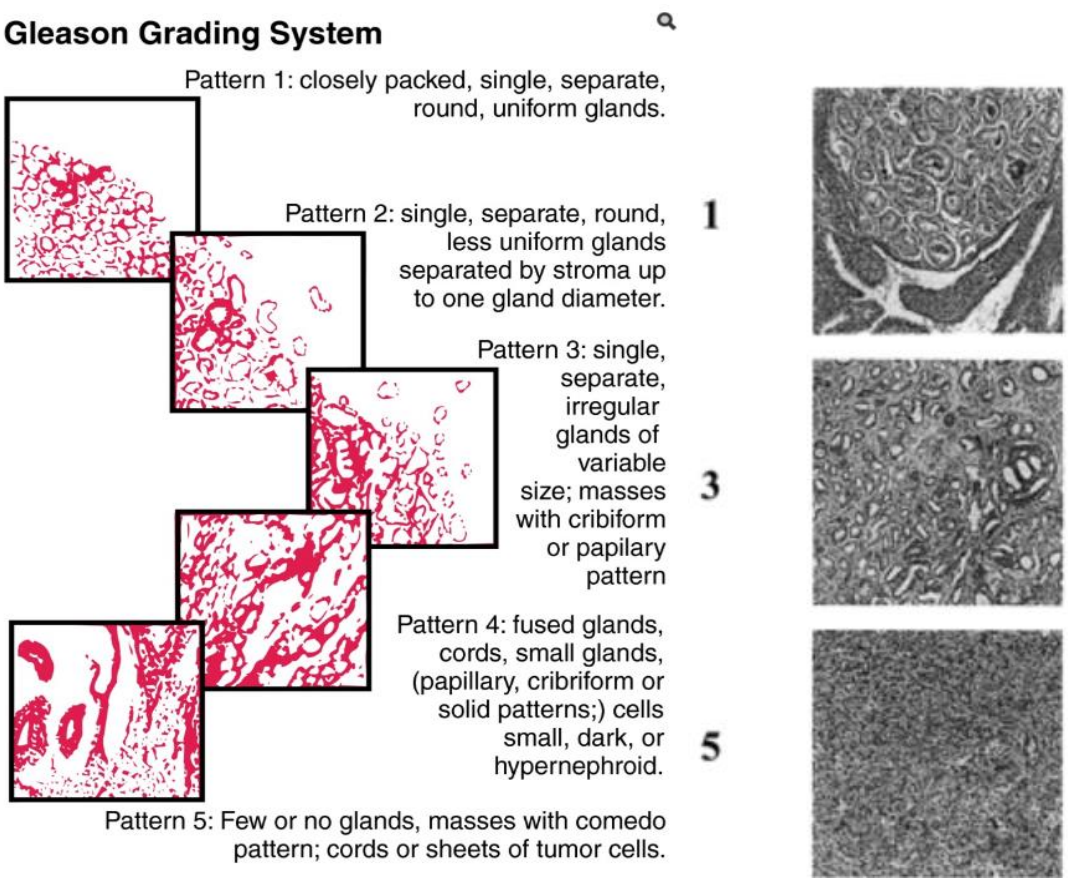

Figure 3. Left: Categorical description of each Gleason score. Right: Histological features found in Gleason grades 1, 3 and 5[1,2].

Grade 1 and 2 samples generally do not raise alarm for concern, as they closely resemble healthy prostate sample. On the other hand, higher Gleason grades are associated with disease state. Starting with Grade 3, the glands begin to appear more variable and irregular in shape, and with Grade 4, fusing of glands are detected, along with cribriform, reduced individual cell size, and darkened sample color. In Grade 5, the entire sample is characterized as being fused together, forming a single-sheet, with little to no lumen present, all indicative of cancerous development[1,2]. In formal diagnosis, the finalized Gleason sum (GS) is concluded by the addition of two Gleason grades most identified in histology samples, with the primary pattern preceding the secondary

pattern. For instance, a GS of 9 could either be reported as 9 (4+5) or 9 (5+4), where the latter case is considered more severe for having Gleason grade 5 as a primary pattern[15,16]. In most medical guidelines, GS 7 to GS 9 are considered as high-grade cancer, thus making the timely and accurate diagnosis of them highly important[17].

1.4 Prostate Cancer: Current Diagnosis

The diagnosis of prostate cancer has several stages. Upon initial suspicion of the risk, the digital rectal examination (DRE) is often issued, in which the physician will physically evaluate the size, shape, as well as the texture of the prostate. During this category of examination, signs such as enlarged prostate, nodules, or tenderness are all considered potential indications of prostate cancer[17]. Along with DRE, blood work is also frequently done to screen for prostate specific antigen (PSA) levels. The traditional cut-off PSA level for risk of prostate of cancer is 4.0 ng/m, above which the patient will be considered at risk for prostate cancer and may be subjected to prostate biopsies[18,19,20]. In spite of the popularity and convenience of PSA screening, much evidence suggests that there is no definitive cut-off level for prostate cancer diagnosis. In a published prostate cancer prevention trial, in a population of 675 men with PSA levels varying between 2-4.0 ng/mL, nearly ¼ of whom were initially diagnosed with prostate cancer, however, most of the individual in this cancer positive group were later cleared from significant risk of prostate cancer after subsequent testing[21]. In fact, it is estimated that the positive predictive value (PPV) for PSA levels over 4 ng/mL is only 30%, while the PPV value for PSA readings exceeding 10ng/mL ranges from 42% to 64%[22]. Having a

false-positive rate often leads to unnecessary biopsies, even overtreatment later on. To prevent the ongoing trend of over-diagnosis and low-sensitivity towards detecting benign prostate cancer cases, recent efforts to reformulate the PSA screening process has shown improved results. For example, the prostate health index (PHI) is a newly developed method, in which PSA derivatives such as total PSA, free PSA, and (-2) ProPSA are all included in the test. Meta-analyses of the PHI have estimated the area-under-the-curve (AUC) value to range from 0.70 to 0.77, which is superior to the conventional PSA test[23]. Another new method called Four Kallikrein Assay (4Kscore) has yielded a higher AUC of 0.82 for detecting cancers with Gleason score equal to or greater than 7. On top of including PSA derivatives, the 4Kscore assay also incorporates measurement of human kallikrein-related peptidase 2, a serine protease that is expressed in distinguished amounts in cancerous prostate tissue and is detected in peripheral blood[24].

1.5 Prostate Cancer: Existing Treatments

Despite initially being localized, prostate cancer can be quite precarious. More than 70 years ago, Huggins and Hodges illustrated the potential effectiveness of hormonal therapy, yet to this day, it cannot act as a complete cure for the advanced forms of the disease due to the heterogeneous nature of the malignant cells involved, including both androgen-dependent and androgen-independent cell types. Androgens are male specific hormones that are known to stimulate the progression of prostate cancer[5]. Androgen-dependent cancer cells can be eradicated using the formerly mentioned

method, often called androgen suppression therapy, where the patients' androgen levels are forcibly reduced via anti-androgen drugs, thus triggering a biochemical cascade that lead the androgen-dependent cells to undergo apoptosis. However, unlike its peer, the androgen-independent cancer cells do not respond to the lowered androgen levels, and becomes responsible for advancing the severity of the disease in spite of suppression treatments. As such, for metastatic prostate cancer, androgen suppression therapy by itself remains ineffective[5,6].

Aside from androgen deprivation, other common treatments involve chemotherapy, radiotherapy, and surgery. Chemotherapy is often carried out in concert with androgen deprivation over a period of several months to 1 or 2 years, with chemotherapy drugs such as docetaxel and estramustine[25]. Radiotherapy consist of projecting conformal radiation doses to specific areas of the prostate, with a reliance on CT scans and MRIs for guiding. Methods such as intensity-modulated radiotherapy (IMRT) and image-guided radiotherapy (IGRT) all fall under the category of radiation therapy[26]. Radical Prostatectomy (RP) is the surgical method in treatment of prostate cancer and is the most popular approach for localized cases in North America. The surgery involves in the entire removal of the prostate gland via robot assistance[27]. Despite the invasiveness of RP, the 5-year and 10-year survival rates of this procedure are reported to be above 85% for all men aged 45 years or older, making it an effective and low risk treatment for localized prostate cancer[28]. The scope of this study will focus on the identifying positive surgical margins (PSMs) during RP, the details of which will be discussed in the subsequent chapters.

1.6 Positive Surgical Margins in Radical Prostatectomy

The purpose of RP is the complete resection of cancerous region, both on eye-visible and microscopic levels. A positive surgical margin occurs when the surgical removal does not achieve the desired thorough removal, leaving residual cancer cells within 5 mm from edge of resected tissue[29].

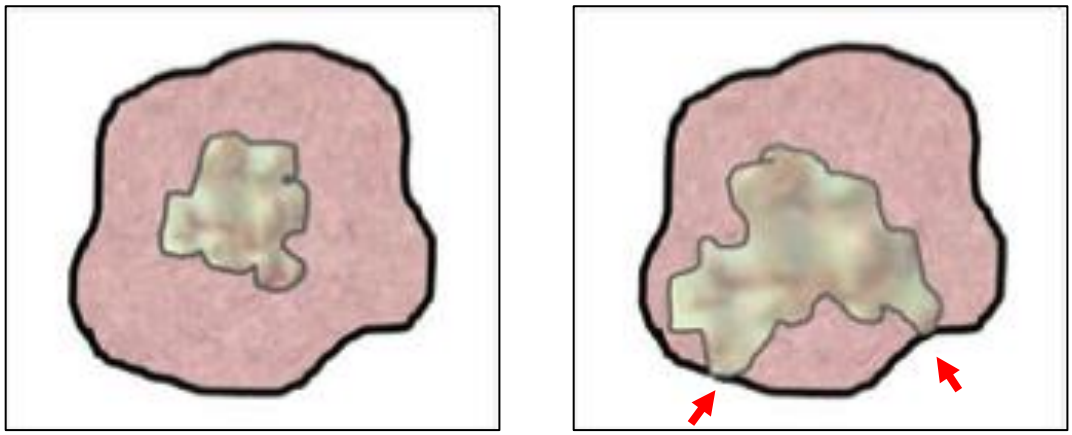

(a) (b)

Figure 4. (a) An excised tumor with Negative surgical margin. The black lines mark the border of the resection, and the tumor cells are entirely contained. (b) Example of two Positive Surgical Margins, marked by red arrows, where cancer cells are found at the surface of the surgical margin[29].

Once the positive surgical margin is discovered after RP, re-excision is required in a secondary surgery to prevent local recurrence of cancer cells, thus increasing stress of prognosis and treatment in terms of financial and physical burdens upon the patient[30]. From an analysis of the National Cancer Data Base from 1998 to 2012, prostate cancer had the highest PSM occurrence in male cancer subjects[30]. Published data estimate that the overall prevalence rate of PSM ranges from 21% to 38%, making PSM a major challenge in improving RP outcomes[30,31,32]. At present, all PSM incidences are confirmed by histopathology, or specifically, intraoperative frozen section analysis. In

spite of this method being the universally standard, it is time consuming, and require at least couple of days after the RP procedure to yield outcomes[27]. For clinical efficiency and reduced patient morbidity, a real time diagnostic tool is much desired, so that PSMs could be identified and removed during the RP surgery, therefore ridding of the need for secondary surgery. This clinical need has sparked a series of research and investigation on Light Reflectance Spectroscopy (LRS), a developing medical imaging modality, and its ability to detect PSM.

1.7 Introduction to Light Reflectance Spectroscopy

Light reflectance spectroscopy (LRS), also commonly called optical reflectance spectroscopy (ORS), or diffuse reflectance spectroscopy (DRS), is a non-invasive optical fiber probe imaging modality that has shown exciting outlooks in fast and real time detection of a variety of cancer tissues, such as breast cancer, cervical cancer[33,34,35]. LRS functions by measuring the light intensity back scattered from the tissue of interest over a range of wavelengths. Although both light absorption and light scattering significantly affect how light travels through tissue, the latter factor vary greatly with respect to the morphological and cellular attributes of tissue, making the LRS spectrum valuable in differentiating between tissue types[27,33]. A series of former studies have already established the effectiveness of LRS in detecting PSM in excised prostates from RP. In a 2014 study, LRS was used in combination with Auto-Fluorescence (AFLS) to examine readings from RD specimens extracted from 37 patients diagnosed with intermediate-to-high-grade (GS ≥ 7) prostate cancer, and by

comparing 724 locations containing benign and cancerous tissues, it was determined via multinomial logistic regression that the dual-modal method can identify GS = 7,8,9 tissue types with 91.1%, 91.9%, and 94.3% accuracy[36]. Although AFLS adds additional insight on differentiating tissue compositions, such as the characteristics of endogenous fluorophores, it was later on discovered that LRS alone was able to effectively distinguish GS ≥ 7 tissue types. A follow up publication in 2016 analyzed LRS measurements from 50 RP specimens, and revealed 91.3% sensitivity and 92.8% specificity towards GS ≥ 7 tissues, proving that LRS by itself is sufficient in detecting intermediate to high grade PSM locations[37].

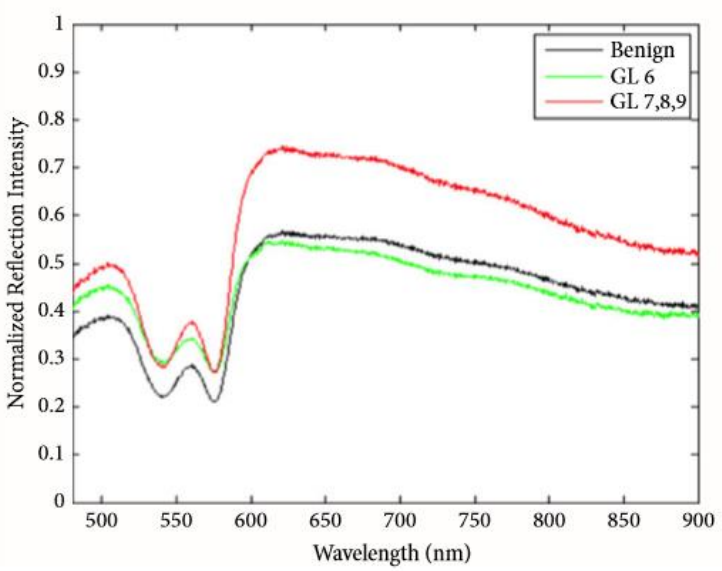

Figure 5. LRS signal illustrating the distinguished reading between benign, GS = 6, and GS =7,8,9 specimens[37].

1.8 Light Reflectance Spectroscopy: Theory

LRS operates by placing the optical probe incident with the target tissue and emitting light into it, as the emitted photons travel through the tissue, they will encounter a number of light scattering agents, whose presence cause the photons to change direction and become reflected back to the tissue surface. The photons reflected back to the surface of the tissue are detected by the photo sensors within the LRS probe, sent to a spectrometer and then computationally processed to yield scattering intensity[38].

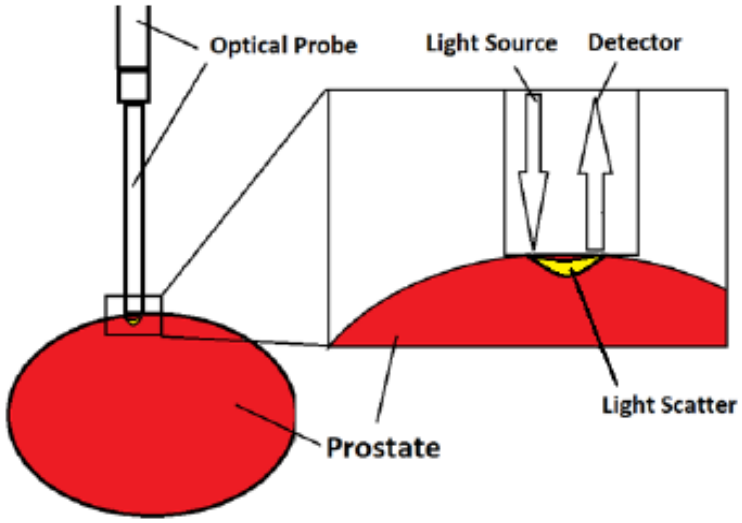

Figure 6. An illustration of how LRS emits light and collects back scattering from the tissue of interest[39].

The factors that primarily influence the intensity of backscattering are chromophores, or light absorbing agents, in addition to cell size and density. The major chromophores prevalent in organic tissue are oxygenated hemoglobin [HbO], deoxygenated

hemoglobin [Hb], and water concentrations [%H2O]. Different quantities of each chromophore affect LRS scattering intensities, generally, higher the [HbO] and [Hb] concentration in a tissue sample, lower the scattering intensities will be from wavelengths 500-600nm. Cancerous prostate tissues experience relative hypoxia compared to benign peripheral cells, and the resultant difference in [HbO] plays a role in LRS's capacity to differentiate GS ≥ 7 tissue types. However, it is the cell size and density within a tissue that most significantly affect scattering, whereby larger and denser cell arrangements, which are uniquely prevalent in cancerous prostate tissues, yield higher light scattering in LRS signals[27,40]. Therefore, the primary features in the LRS spectrum that distinguish normal and cancerous cells are the reflectance, or scattering, intensities, and differences in slope. As seen in Figure 6 above, the most noticeable difference between the normal and cancerous prostate tissues is that the latter returns higher reflectance intensities across a wide range of wavelengths due to its larger and more closely packed cells.

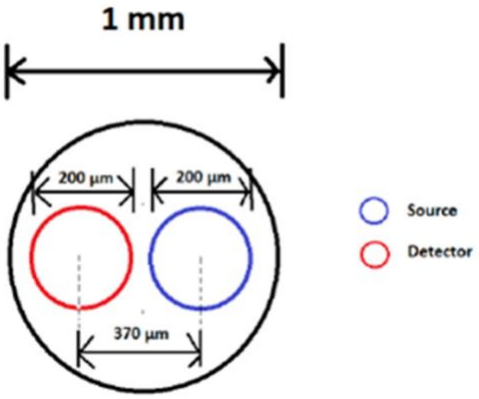

Figure 7. The cross-section of the LRS optical probe utilized in this study. The essential fiber components, the light source (blue), and the detector (red), are sheathed within a metal sleeve. At the tip of the probe, both fibers are sealed by a thin layer of transparent lens[39].

The physical attributes of the LRS probe itself affect its optical capacity. Thicker fibers and higher fiber separation distances reveal optical information deeper inside the tissue, while thin fibers combined with small fiber separation distances prevent the emitted light to propagate deep within the tissue, and thus are able to investigate closer to the tissue surface, which is better suited for positive surgical margin detection. The LRS probe deployed in this study are configured with 200-micron light source and detector fibers, and a 370-micron separation, which altogether exhibits shallow light penetration past the tissue surface (refer to Figure 7 above).

1.9 Light Reflectance Spectroscopy: Equipment and Limitations

The current LRS equipment used PSM detection studies include an optical probe with 200μm light source and detector fibers, a tungsten-halogen light source (HL2000HP, OceanOptics, Inc., Dunedin, FL), and a modular spectrometer (USB2000+, OceanOptics, Inc., Dunedin, FL).

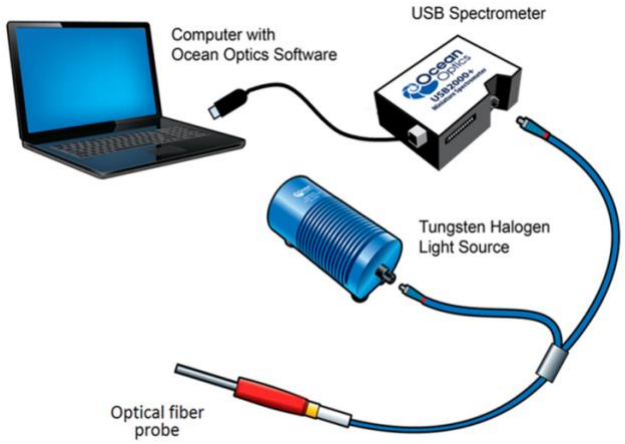

Figure 8. The LRS equipment for PSM detection: the optic probe is connected to both the light source and the spectrometer, and the spectrometer relays the scattering signal to the computer[41].

The software used to view and save the LRS data is called OceanView, which is also developed by OceanOptics, Inc. To setup the equipment, the two inlets of the optic probe will be separately connected to the tungsten-halogen light source and the spectrometer. The light-source device delivers photons into the source fiber within the optic probe, while the spectrometer picks up the tissue-reflected backscatter from the probe's detector fiber, digitizes the signal, and sends it into the computer for viewing and analysis.

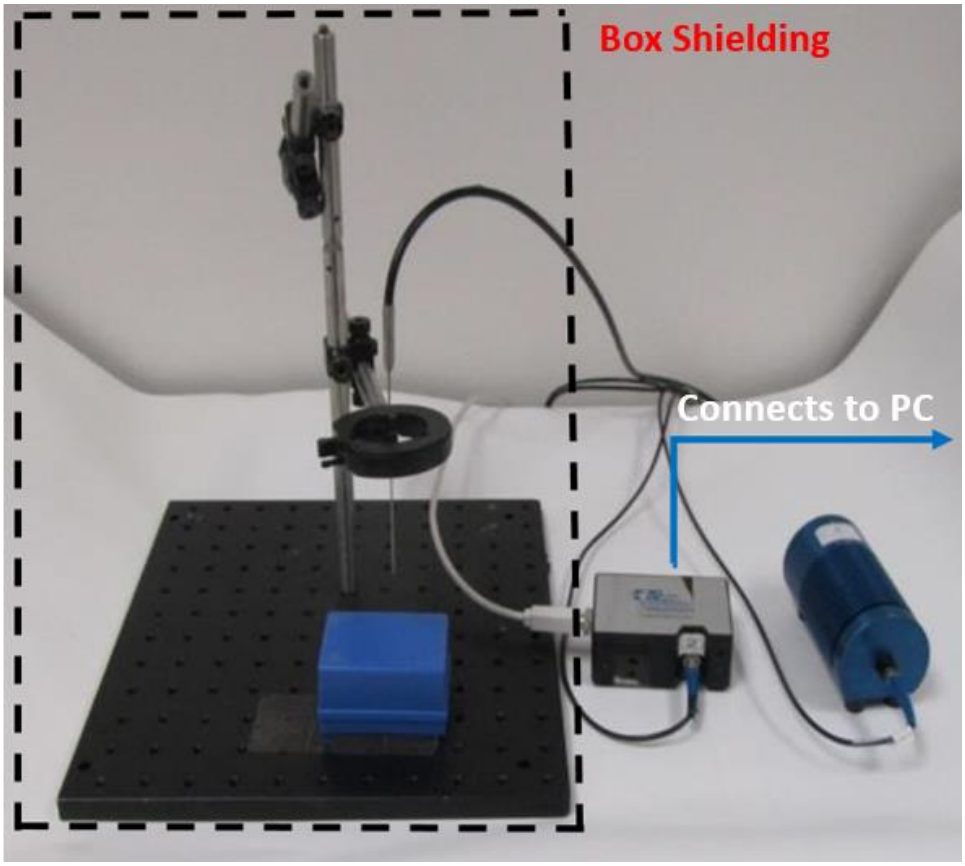

Figure 9. Equipment setup for data collection, the optic probe is held securely by a clamp and then fixed on an imaging stage. The entire stage sits within a black box (not shown, illustrated by dashed black lines) to shield signal from external noise. The blue cube underneath the needle probe is a mock sample[37].

The figure above depicts the configuration of the LRS equipment during testing. In order to collect reflectance reading for a single location on the tissue sample, either the clamp or the needle must be first lowered to meet the surface of the tissue, then the box shielding will be closed to completely block out environmental lighting, which generates noise in the LRS signal, for the photons emitted by the ambient light sources will also penetrate the tissue and elicit additional backscattering, and consequently contaminates the signal intended to reveal only the optical properties of the tissue in response to the probe's light source itself. The real-time signal is displayed on the computer via OceanView, and once the probe is set in the desired location along the sample and shielded properly, the user will manually click on the "save" button in OceanView to store the one spectrum data point, containing the intensity values from 480 to 1200 nm. The current procedure for LRS data collecting has two major draw-backs that undermines the LRS's advantage of real time data streaming:

1. Lack of efficiency: since the LRS probe can only examine a very small area (~1 mm^2) of tissue at a time[33] , and assuming that each excised prostate would require inspection from at least 10 to 20 different locations, the current protocol of adjusting the stage, rotating the prostate, stabilizing the probe on the prostate, then finally turning over to the computer screen to save data is grossly inefficient, failing to achieve immediate positive surgical margin detection, not to mention its delaying of the RP surgery completion time if it was implemented at its current developmental stage.

2. Bulkiness: having a sizeable box and fixing the optical probe onto a stage increases the inconvenience of data collection. Between each data point, the user has to reach inside the box to adjust the probe and rotate the prostate specimen, the act of which is marked by limited range of motion for both the hands to maneuver and the probe to shift or rotate. Therefore, having the box shielding not only limit mobility, but also increase the time required to fully examine a single prostate specimen for PSMs.

1.10 Purpose and Workflow of Thesis:

The goal of this project is to devise new methods to circumvent the challenges facing the current LRS system and to test their viability towards enhanced user-friendliness and efficiency. In response to the shortcomings mentioned in the previous section, the concept of incorporating the LRS probe into a shielded handheld device was conceived. Once secured within a proper casing, the optic could be operated in a stylus fashion: simply point and touch. If successful, current reliance on the stage and box shielding could be eliminated.

Another objective of this project is to minimize computer interaction during data collection. While operating the existing system, the user first fixes the optical probe at a desired location, then turns to the computer to view and save a snapshot of the live data, with the latter step not interfering with the stability of the former. However, once

configured to a handheld system, after the user pins the optical probe onto a location on the sample, it would be extremely difficult to maintain a constant pressure and angle of contact while he/she has to reach with the other hand to interact with the computer for a snap shot of the data. The incorporation of a tactile switch into the handheld device was proposed as a solution to this problem, whereby triggering the switch will allow the user to clip snap-shots of the live LRS signal and save them as numerical data.

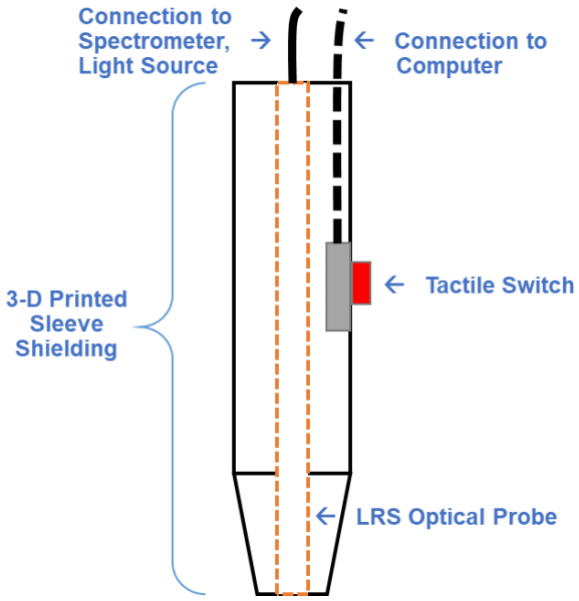

Figure 10. Diagram depicting the overall concept of the novel device, which will operate similar to a stylus. The optic probe itself will be encapsulated in a 3-D printed shielding, with its inlets connected to the light source and spectrometer (feeds data into the computer) as always. The tactile switch will be connected to the computer, and its activation/deactivation will allow the user to directly control the acquisition of incoming LRS data without interacting with the data processing software.

It is not clear how well an external casing can shield the LRS signal from noise induced by ambient lighting. In addition, if handheld, human error would inevitably play a factor in contributing to the consistency of data collecting, as the slightest movement of could alter both the intensity and shape of the LRS spectrum. In this study, the concept of a handheld LRS probe device was tested by securing the probe inside a series of 3-D

printed black sleeves that act as different modes of shielding. The sleeved LRS probe configurations were tested against the traditional method in the following aspects: a) Sleeve diameter. b) Probe retraction depths (how far the LRS probe sits away from the tip of the sleeve casing). c) Light conditions. d) Stage vs. handheld configurations. Additionally, comparative testing was carried out between two LRS probes, one of which was used in previous studies, and it is dual-modal with LRS-AFLS (Light Reflectance Spectroscopy combined with auto-fluorescence) fibers in its construction, giving it extra connector inlets that are unneeded and inconvenient for testing and overall device construction.

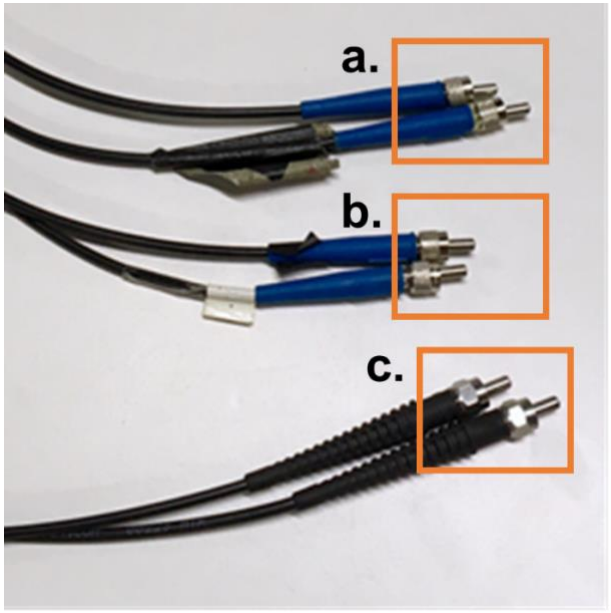

Figure 11. The connection inlets of the old dual modal probe (in blue), and the new LRS probe (black). (a) The old probe's connections for auto-fluorescence, which are no longer used in detecting PSMs in this research. (b) LRS's connections for the old probe. (c) New LRS probe's connectors.

The new optical probe only contains LRS fibers in composition, and is the candidate for replacing the older dual-modal probe. However, to determine whether the data from the

new probe can be correlated to the PSM data bank formerly established by the old dual-modal probe, comparative tests must be conducted between the new and old probes, which was carried out in this project and will be discussed in the upcoming sections.

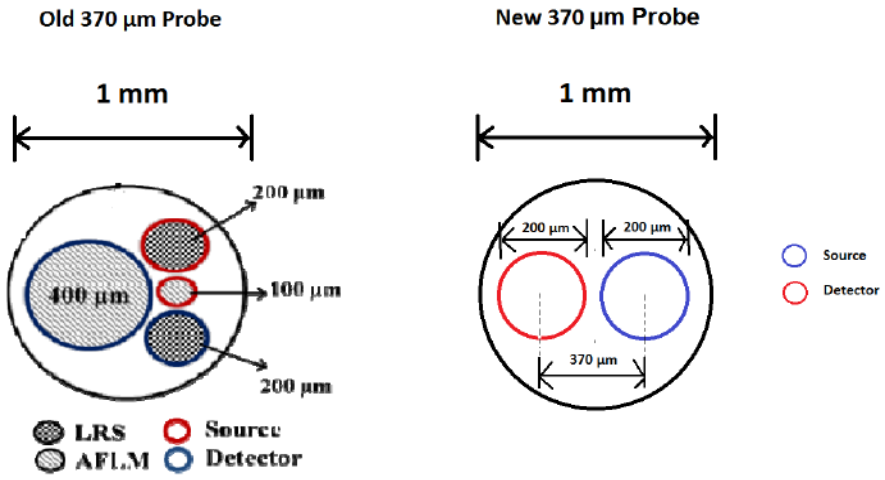

(a) (b)

Figure 12. The cross-sectional diagram of the old (a) and new (b) LRS optic probes. In terms of LRS components, both the new and old probe are specified to contain 200 µm source/detector fibers, which are separated by a distance of 370 µm within each probe. However, despite their specifications being identical, thorough testing and calibration are still needed to ensure that the spectra produced by both probes are not significantly different[39].

In chapters 2, 3, and 4, the experimental methodology, the testing results, and the discussion of the results will be described in detail, respectively. And in chapter 5, the design process undertaken during this project will be outlined, namely with respect to the switch set up and programming and the physical design of the handheld casing itself.

Chapter 2: Methodology

2.1 Black Sleeves as Alternate Shielding: Initial Testing

To mimic the environment of a shielded, handheld device, simple black sleeves were designed and 3-D printed in accordance to the dimensions of a new LRS probe. The rationale behind the use of a black sleeve is to provide shielding, and if successful, the previously bulky box shielding could be replaced.

During the first round of testing, tuna meat spectral data was collected with the new LRS probe under 3 different configurations: 1) Full exposure to room lighting 2) Box shielding 3) Sleeve shielding.

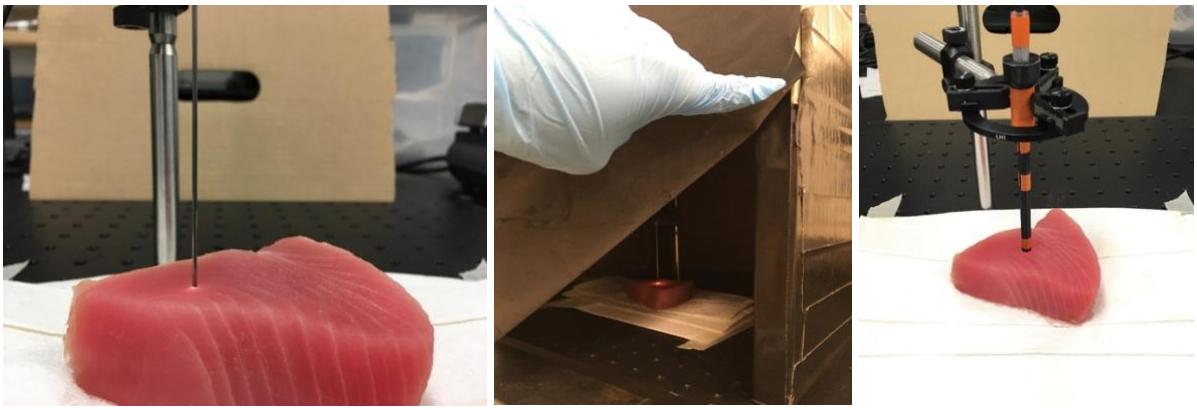

(a) (b) (c)

Figure 13. (a) The unshielded probe on tuna sample. (b) Probe with traditional box shielding. (c) Sleeve shielded probe.

The sleeved testing group has two subgroups, one utilized a sleeve with an internal diameter of 1.5 mm, while the other 4.0 mm. Note that despite their internal diameter differences, the external diameter of both sleeves was set to be identical at 6.3mm. The

aim behind the varying the internal diameter of the sleeve was to investigate whether larger internal cavity space (sleeve with 4.0mm internal diameter) in a shielded environment is superior to having none, as the traditional box shielding provides a large empty cavity, and functions optimally in shielding noise.

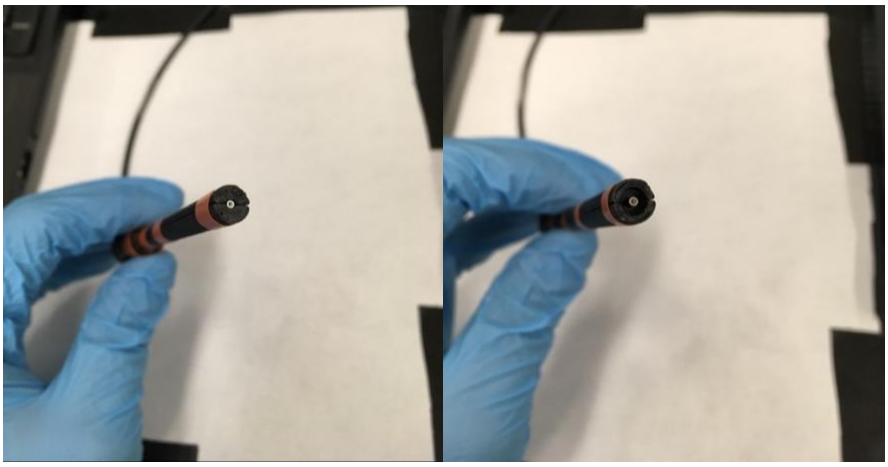

(a) (b)

Figure 14. (a) Sleeve with 1.5mm internal diameter (2) Sleeve with 4.0 internal diameter.

(a) (b)

Figure 15. Illustration of the differences between 1.5 mm and 4.5 mm internal cavity diameter. (a). Sleeve with 1.5 mm internal diameter. (b). 4.0 mm sleeve.

All groups were fixed by stage and clamp. A total of 10 spectra was collected and averaged for each group along the lean portions of the tuna sample, in between the ordered striations of fat. The justification for the selection of ahi tuna as a tissue sample

resides in its superior consistency compared to other common types of meat i.e. pork, chicken, and beef, for it is difficult to account for the optical differences between individual locations along the formerly mentioned tissue types, and when collecting LRS data points across their surfaces to compare between the testing groups, a larger margin of error would occur in the comparison result due to each group having potentially measured areas with significantly dissimilar optical properties. Tuna is also a good candidate for having high firmness, which is also a physical characteristic of the prostate gland.

2.2 Black Sleeves as Alternate Shielding: Sleeve Diameter

In further investigation of how applying a sleeve would perform as shielding, black sleeves with larger overall diameters were 3-D printed, and compared to the first generation sleeve with 6.3 mm overall diameter. In this test group, all sleeves' internal diameters were set to 1.5 mm for consistency. The purpose behind this experiment was test whether increasing the sleeve coverage on tissue sample could yield to enhanced shielding effects. The experimental procedure was identical to that in section 2.1.

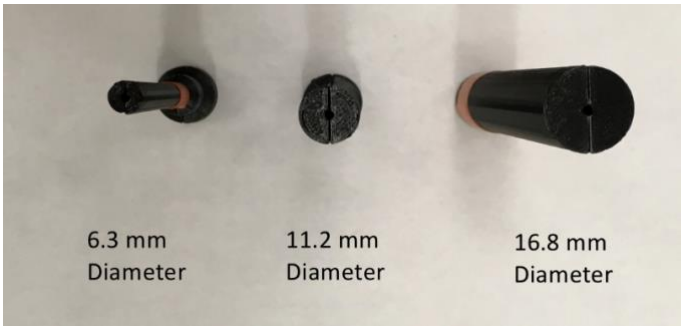

Figure 16. Side by side comparisons of sleeves ranging from 6.3mm to 16.8 in diameter.

2.3 Black Sleeves as Alternate Shielding: Low vs. High Light Conditions

Aside from deploying sleeves, a separate approach was devised in response to the shielding issue. It was tentatively speculated that total darkness in the surrounding environment is not required in order for LRS probes to function noise-free. Therefore, two probe configurations, bare and sleeved, were tested on meat sample under 3 distinct light conditions: 1) Lack of environmental light, which is created by the application of the traditional box shielding 2) Normal fluorescent light, full brightness 3) Dimmed room lighting (by 50%), in which the light emitted by the optical probe appears significantly brighter than the surrounding light emissions.

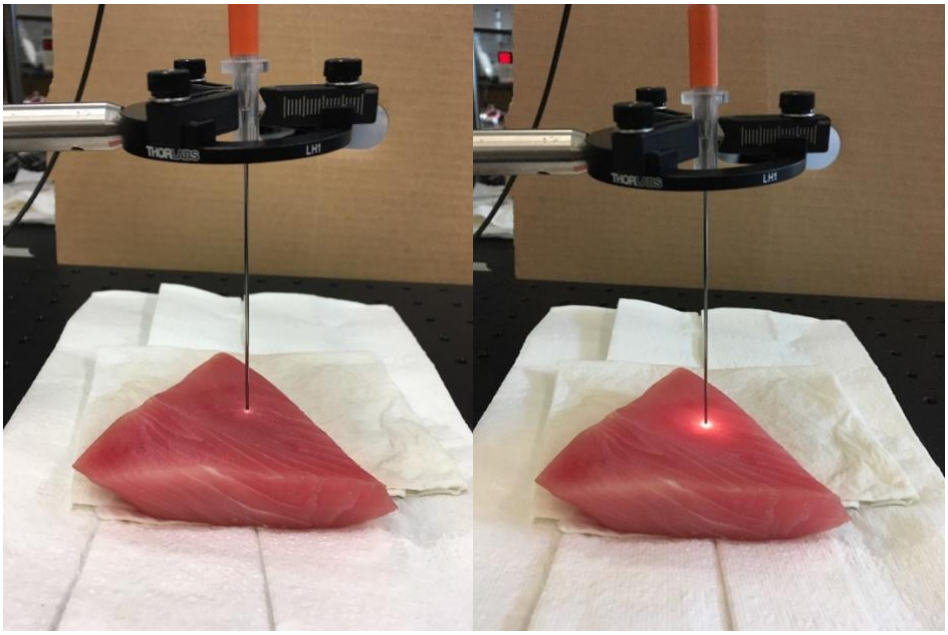

(a) (b)

Figure 17. (a) LRS probe under normal room brightness (b) LRS probe under reduced room brightness. Note that dimmed brightness was created by reducing the number of bulbs being switched on, not by turning off all of the light.

2.4 Black Sleeves as Alternate Shielding: Varying Sleeve Retraction Depths

While all of the preceding experiments involved the usage of sleeves whose length ran nearly coincidental to the tip of the probe, allowing the encased probe to make contact with target tissue, in this additional round of testing, longer sleeves were 3-D printed so that once the probe is secured within, its tip will not directly touch the meat sample during data collection. The initial speculation was that if the probes do not physically touch the tissue sample's surface, the chance of the probe penetrating too deep into the sample as a result of being handheld could be reduced, and thus decreasing the overall human error. The most significant difference in this experiment is that contrary to previous tests, the sleeved probes were handheld while spectral data was being collected. The data collection routine consisted of handholding each sleeved probe until the sleeve tip touched the surface of tissue, and then saving a snap shot of the returned spectrum. The same process was repeated 10 times for each group on the same tissue location for consistency. Each group's mean was plotted with its standard deviation.

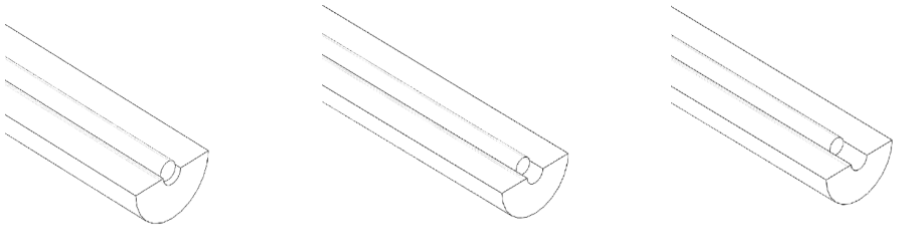

(a) (b) (c)

Figure 18. (a) 0.5mm retraction, which was implemented in all previous experiments, where LRS probe being close enough the edge of the sleeve to touch the tissue sample. (b) 1mm retraction. (c) 2mm retraction. The latter two groups do not allow the probes to come into direct contact with the tissue.

2.5 Optic Probe Comparison: Liquid Phantom Experiments

In order to simultaneously compare signals from both the old and new optic probes in a controlled fashion, tissue samples with consistent optical properties is desired. However, due to the non-uniform texture of most tissue types, it would be difficult to eradicate the consequential errors. Therefore, to mimic the basic optical properties of biological tissue, the decision was made to deploy blood-intralipid phantom in this comparative testing. While the blood will provide the Hb, HbO, and H2O as variables affecting light absorption, the intralipid will act as the variable affecting light scattering. The type of blood utilized was defibrinated horse blood (Hemostat Laboratories), which is commonly used in vitro diagnostics. The intralipid selected is an intravenous injectable fat emulsion with 20% soybean oil (Intralipid®20%, Fresenius Kabi), and it is sterile and balanced to pH = 8. The experiment consisted of sequential addition of 2 mL portions of horse blood, up to 10 mL in total, for 5 sets homogenously mixed intralipid solutions with varying intralipid concentrations (from 0.5% to 1.3%). After each round of horse blood addition, the LRS spectrum was captured. The total volume of each solution is fixed at 800 mL, and based on the intended overall intralipid concentration, the amount of intralipid and water was calculated and listed in Figure 19 below. Note that both the horse blood and intralipid are perishable and were refrigerated after opening and before usage.

At the beginning of each experiment set, the diluted intralipid solution was first made by adding the appropriate volumes of intralipid and water, using graduated beakers, into a 3-D printed, black colored reservoir designed to hold a maximum of 1000 mL. While

holding a total intralipid-water mixture of 800 mL, the liquid level should be ~ 3 cm below the brim of the reservoir.

Total Volume: 800 mL		
Overall Intralipid Concentration	**Intralipid (mL)**	**Water Volume (mL)**
0.005	20	780
0.007	28	772
0.009	36	764
0.011	44	756
0.013	52	748

Figure 19. A Table listing of amount of water and intralipid needed for each diluted concentration, from 0.5% to 1.3% of the total solution volume (800mL).

Once the intralipid and water have been added to the reservoir, the solution was to be set under constant magnetic stirring. As seen in Figure 20, Both the new and old probe were fixed by clamp and stage and submerged exactly 1 cm into the solution. The exact 1-cm submersion of the probes are achieved by initially wrapping tape 1 cm above their tips while using a ruler as reference. Once secured onto the stage, the clamp holding each probe was lowered until the bottom edge of their attached tapes have touched the liquid surface. Note that the black box was used to cover the set up to shield the LRS signal from noise. Before the first addition of horse blood, the solution was first stirred on medium-high speed for 2 minutes, after which the speed was reduced to low and allowed to sit until no vortex formation was found. Then, while the solution was under low stirring, 10 sets of LRS spectra was collected from each probe as baseline.

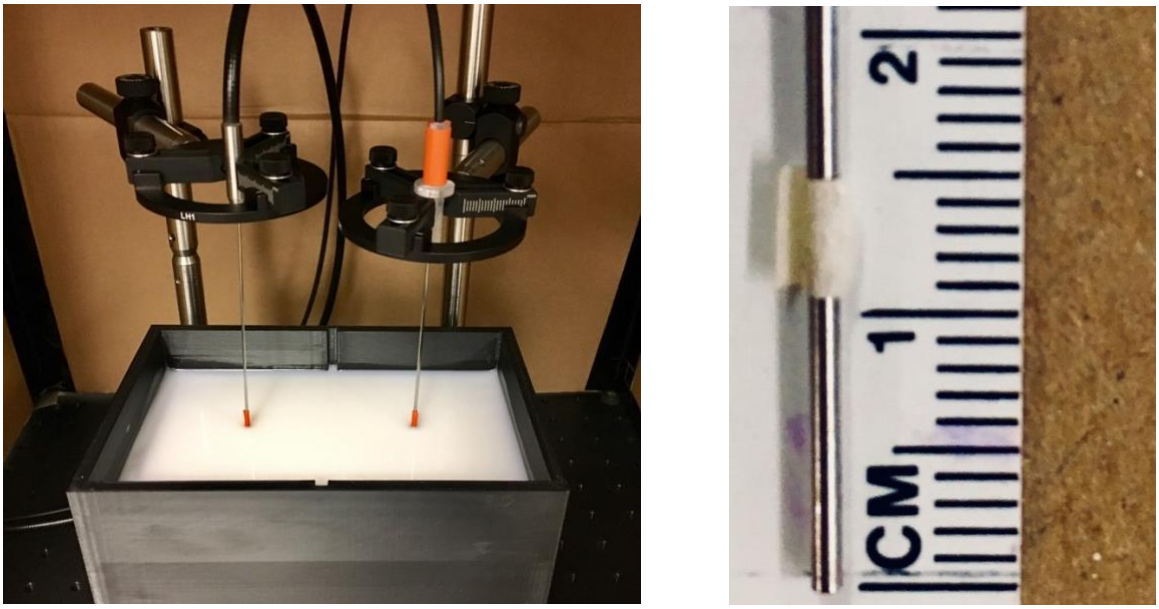

(a) (b)

Figure 20 . (a) The old (left) and new (right) LRS probe being submerged into the intralipid solution, before the adding of horse blood. The magnetic stirring (not shown), sitting below the reservoir was kept on throughout the experiment to keep the solution homogenous. (b) Photograph demonstrating the tape being attached 1 cm above the optic probe's tip.

Subsequent to collecting the baseline readings, the first 2 mL addition of horse blood was added via a 5 mL syringe. Then, the stirring was tuned up to medium-high for 2 minutes, after which, it was reduced to low once more, allowed to sit for 30 seconds, before the spectra (10 sets for each probe) were collected under low stirring. The former steps would be repeated for every subsequent additions of blood.

Once a total of 10 mL of horse blood was added and the corresponding spectra was collected. The solution was mixed with 100 mL of 1% household bleach for 30 minutes before disposal. The probes were cleaned with film paper, dabbed in 70% isopropyl

alcohol. The spectral data collected purely from the intralipid-blood phantom was also normalized through a well-established method called “white sample calibration”, where both probes’ are separately set in contact with a white calibration medium (Ocean Optics, Dunedin, FL) and had each of the resulting spectra collected and averaged. This practice is based on the widely accepted model by Zionos and Dimou[38]:

$$R_p = \frac{1}{k_1 \frac{1}{\mu_s'} + k_2 \frac{\mu_a}{\mu_s'}} \quad (1)$$

The model equation above describes a verified relationship between a tissue sample’s optical reflectance (R_p), reduced scattering coefficient (μ_s’), and reduced absorption coefficient (μ_a). Parameters k1 and k2 are fixed, and primarily describe the internal geometry of unique to each optical probe and the spectrometer system. R_p is obtained by dividing “R,” the reflectance collected from the white sample. Doing this, the spectral effects due to the physical composition of each probe is factored out[38,40].

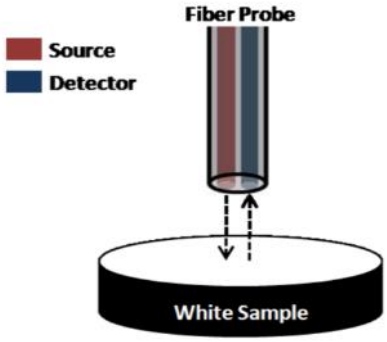

Figure 21. An illustration of the white calibration process. In practice, the probe contacts the sample[40].

Chapter 3: Results

3.1 Initial Testing for Sleeve Shielding

Among all four groups' scattering signal collected from tuna tissue, only the traditional box shielding yielded a smooth averaged spectrum that is marked by absence of any noise artifacts. Moreover, the data indicates no significant difference between sleeves of varying internal cavity sizes.

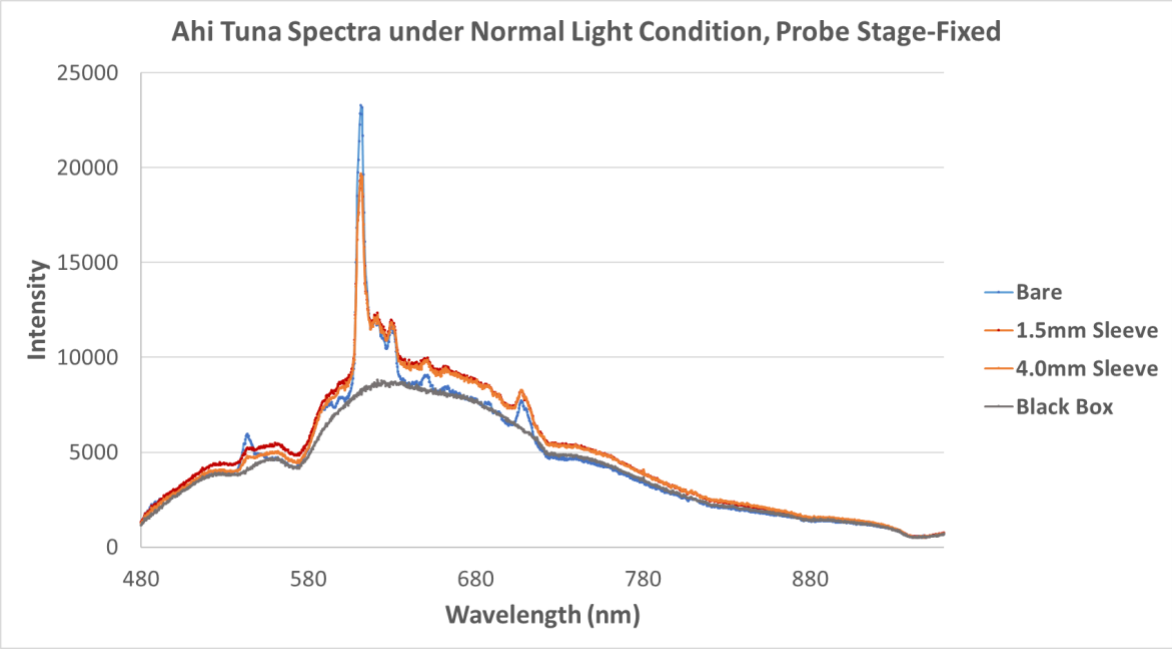

Figure 22. Averaged scattering intensity spectra from four probe configurations. Box shielding displayed the optimal shielding ability.

3.2 Sleeve Testing: Diameter Variations

Contrary to speculations, the results suggests that significantly increased sleeve diameters does not bring significant increases in shielding capacities.

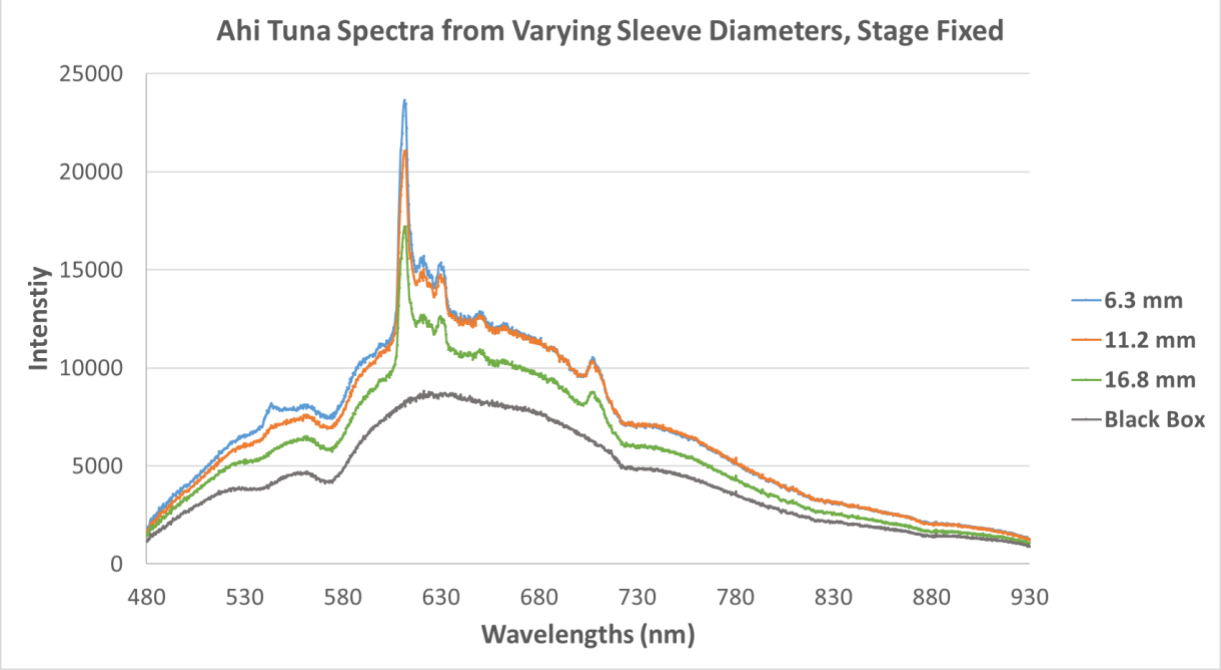

Figure 23. LRS spectra from tuna tissue. Although the 16.8mm group displayed slightly reduced noise intensity (major spike at ~600 nm) when compared to the thinner groups, it cannot achieve the same level of shielding as did the box shielding.

From Figure 23, it can be seen that while the bare probe yielded the highest noise intensity, the probe in black box returned no noise spikes at all. Both of the former test groups act as controls whose responses were well-predicted. And the trend seen among the sleeve groups is that despite shielding effects improved linearly with respect

to larger sleeve diameters, none of them were able to yield spectra without significant noise.

3.3 Sleeve Testing: Low vs. High Light Conditions

By reducing the amount of light present during testing, even if there were still external light present, the strength of the noise spikes were dramatically decreased.

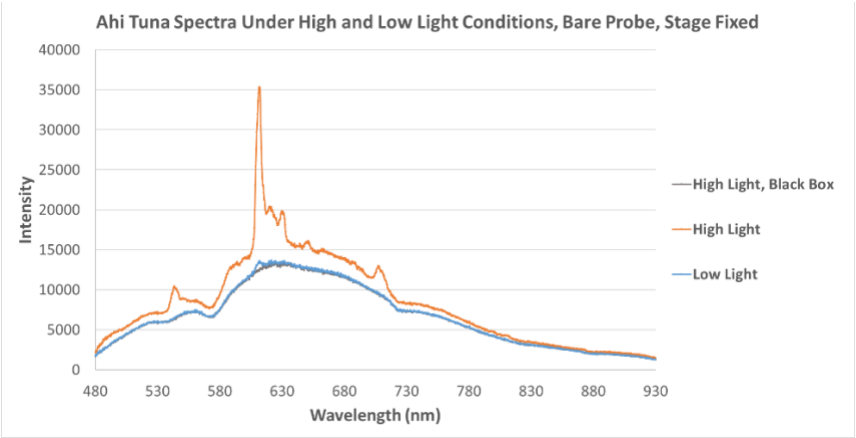

(a)

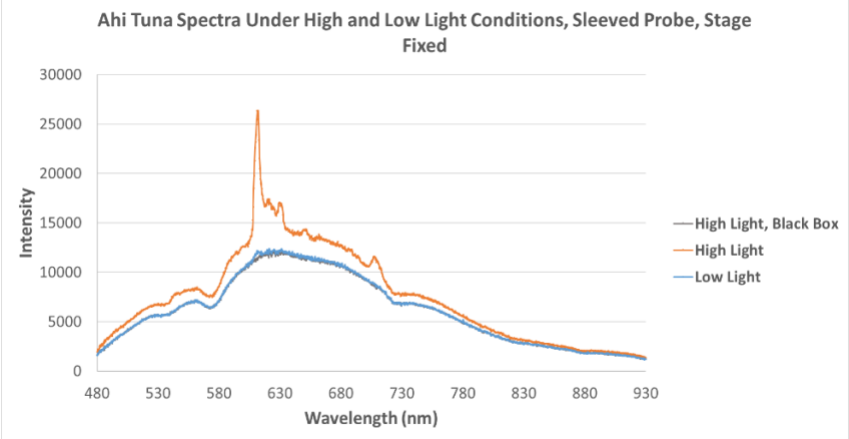

(b)

Figure 24. (a) Bare LRS probe in dark, light, and dimmed conditions (b). Sleeved LRS probe under identical light conditions.

In dimmed light conditions, there exists little to no distinction between the sleeved and naked probes, the noise from both configurations were significantly reduced to the point where they closely resemble the noise-free signal produced by the black box.

3.4 Handheld Sleeve Testing with Varying Sleeve Retraction Depths

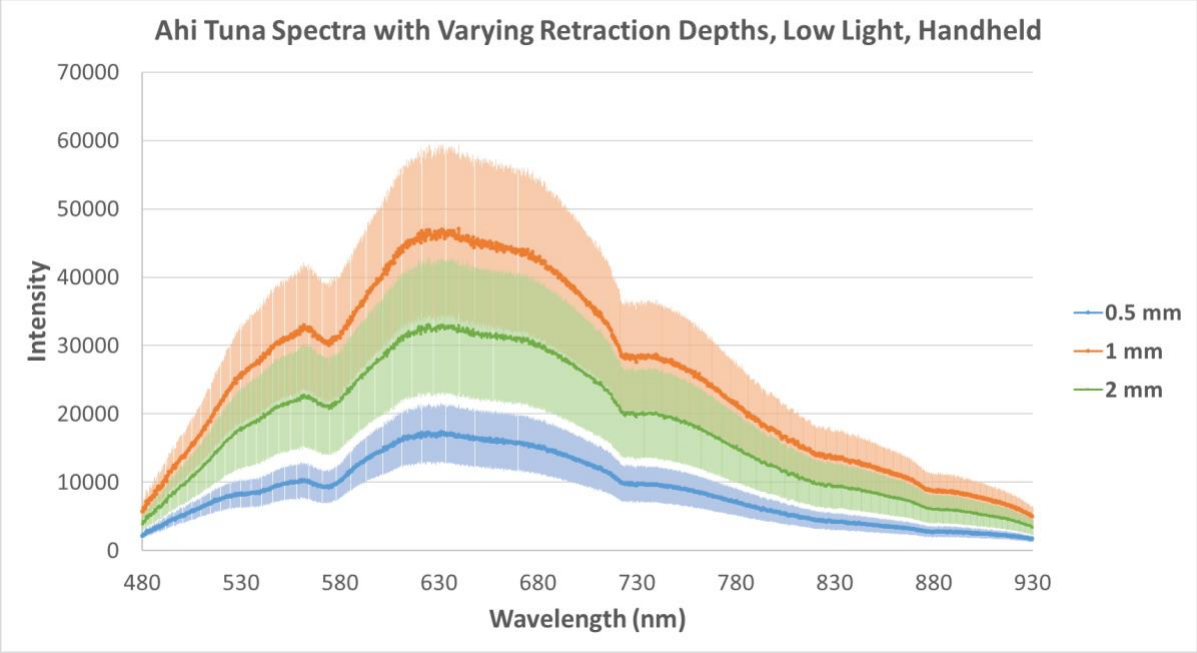

Figure 25. Averaged spectra for all three retraction distances, standard deviation included. The error was of the highest magnitude in the 1 mm retraction group, and lowest in the 0.5 mm retraction group.

In the handheld experiment's plotted data, sleeve groups with longer retraction distances, 1 mm and 2 mm, yielded higher intensities and deviation, with the former having the largest magnitude overall.

3.5 Probe Comparison in Liquid Phantom

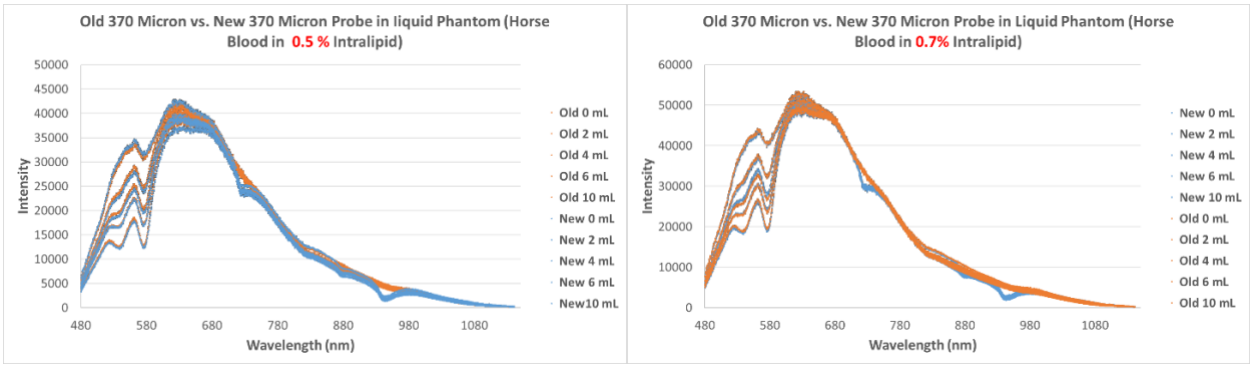

(a) (b)

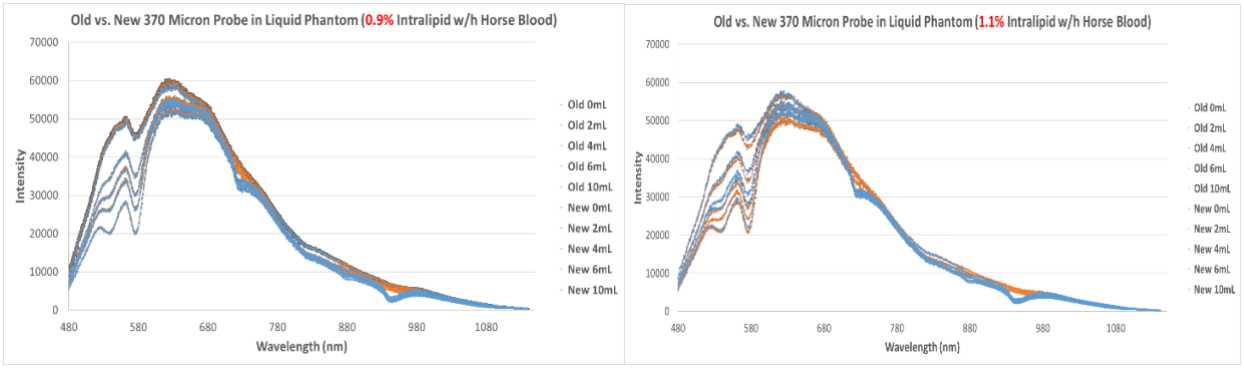

(c) (d)

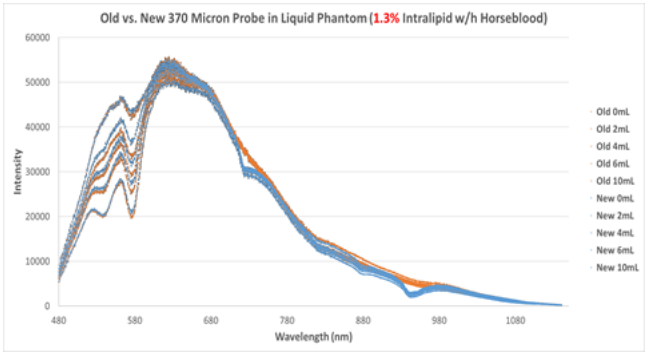

(e)

Figure 26. The following are the raw spectra between the old (orange) and new probe (blue). (a) 0.5% intralipid spectra (b) 0.7% intralipid spectra (c) 0.9% intralipid spectra (d) 1.1% intralipid spectra (e)1.3% intralipid spectra. Every single curve on each graph is the mean of 10 distinct readings.

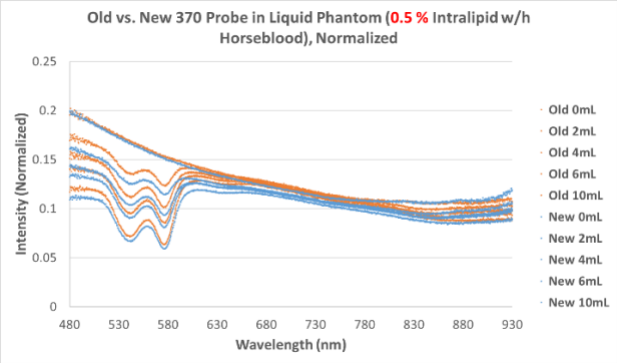

(a)

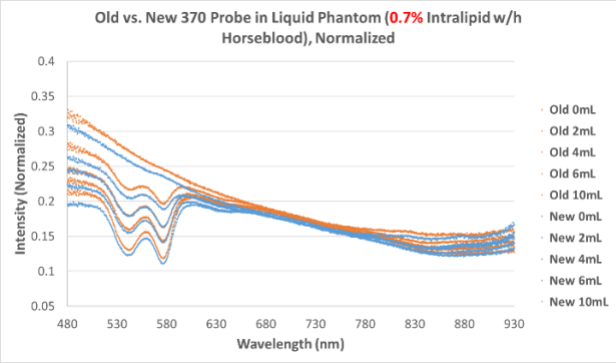

(b)

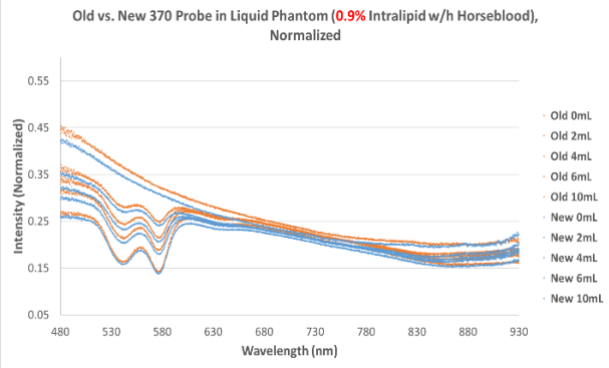

(c)

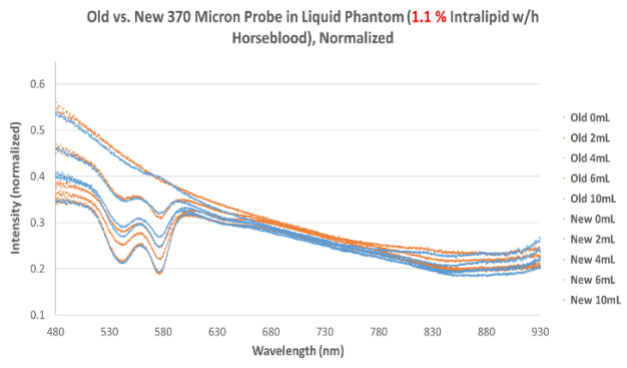

(d)

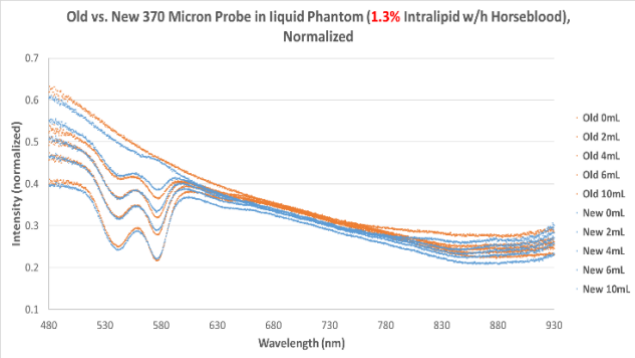

(e)

Figure 27. The following are white-sample normalized spectra between the old (orange) and new probe (blue). (a) 0.5% intralipid spectra (b) 0.7% intralipid spectra (c) 0.9% intralipid spectra (d) 1.1% intralipid spectra (e) 1.3% intralipid spectra. The normalization process is done by dividing the phantom spectra of both probes by that from the white-sample.

A general pattern is seen among the spectra across all concentrations tested, in which the new probe's intensity is slightly lower than that of the old probe, particularly seen in the white-sample-normalized group. While both the spectra slopes are nearly identical for both groups in regions ~750 nm and above. The hemoglobin absorption (500-600nm) region demonstrated more distinctions between the two LRS probes.

Chapter 4: Handheld Device Design

4.1 Overall Device Concept

Based on the results from earlier experiments, it was concluded that in order for the LRS probe to function optimally inside a handheld casing, the following conditions would have to be sufficed in tandem:

1) Dimmed light intensity in the operating environment: from the sleeve shielding experiments, it was gathered that the complete lack of light is un-needed for noise-free LRS signals, instead, while the intensity of the ambient lighting has been reduced so that the probe-emitted light becomes the predominant light source penetrating the target tissue, the resultant LRS signal would be free of noise.
2) Direct contact with tissue: contrary to the initial hypothesis, the sleeve retraction experiments illustrated that while the optical probe was fixed at 1 and 2 millimeters above the tissue sample, the LRS signal varied more significantly in response to the movements and pressure variations induced by hand operation. Therefore, to minimize the signal's variability, it is concluded that the LRS probe remain contact with its target sample as it did in traditional setup.
3) Minimized interaction with computer during data saving: by properly installing and programming a tactile switch, the resultant device's data can be collected by only pressing on the switch.

Of the two critical conditions mentioned above, the dimmed ambient light environment could be created by either shutting off the overhead light bulbs, and placing a small lamp at a proper distance from the LRS set up, or simply dial down the light intensity controls in facilities that are equipped with more advanced light controls. In terms of allowing contact between the optical probe and the sample, the 3-D printed sleeve casing with 0.5 mm retraction distance can be implemented in the overall device design to allow probe-tissue contact. Diameter of the sleeve tip is kept minimized for provide better accuracy while aiming, as in this case, the incorporation of the sleeve is purely for the purposes of forming a protective barrier, and not to provide shielding from external noise.

The results from section 3.4 suggest that in dimmed ambient light conditions, the presence of shielding would make no significant difference as compared to leaving the optical probe entirely unprotected. From this finding, it may sound logical to leave the optic probe exposed in the device design. However, by inspecting the physical condition of the older LRS probe, a noticeable bending was observed, suggesting that its thin, needle-like construction is prone to damages under repeated use. Thus, from the perspective of durability and stability, the sleeve shielding was kept as a major aspect of the device design. In addition, since no significant difference was seen in the LRS readings between the sleeved and bare probe configurations (refer to section 3.3), concerns with regard to sleeve-induced signal disruption can be eliminated.

To satisfying design parameter 3), which is to minimize the computer interaction, the use of a tactile/push-button switch was considered the most simple and viable approach. On top of a 3-D printed sleeve casing to encase the optical probe, a

miniaturized tactile switch will be attached to the exterior of the casing, where upon a click of the button will signal the computer to save a snapshot of the live LRS signal.

4.2 Configuration of Device Components

The tactile switch chosen as a part of the device design is an (OFF) - ON type push button switch (KSC721GLFS, C&K Components, Inc., Newton, MA) with Gull Wing terminals, with simple construction and small dimensions that allow easy incorporation.

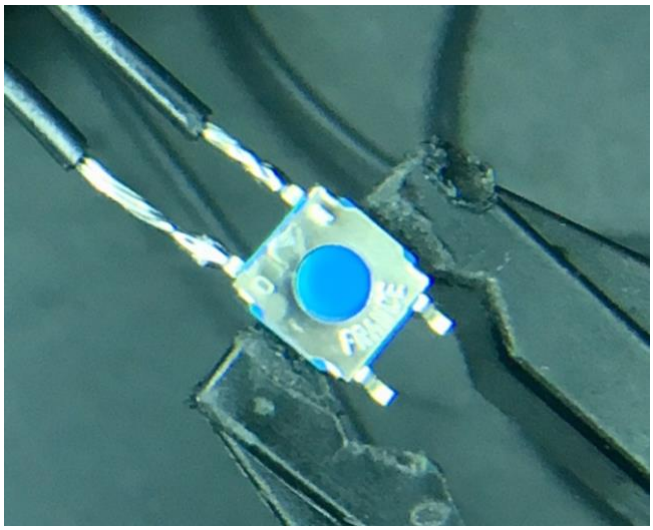

Figure 28. The tactile switch soldered with the insulated copper wires at its input and output terminals.

To interface with the LRS software on the computer, the switch was first soldered with a pair of 22-AWG stranded insulated copper wires (ST2225BK, Shaxon Industries Inc., Anaheim, CA), which was then connected to the digital input/output terminals of a data acquisition module (USB-6002, National Instruments, Austin, Texas). In this arrangement, the data acquisition module (DAQ) helps to complete a circuit that outputs

either an “ON” or “OFF” condition signal to the computer, which with additional programming, will either start or stop the processing of live LRS data by the application software to be viewed and finally saved.

Once the tactile switch was successfully configured, the handheld casing components were designed in SOLIDWORKS® and 3-D printed using a Fused Deposition Modeling (FDM) printer (PolyPrinter 229, PolyPrinter, Midlothian,TX). Consequently, the tactile switch and the LRS optical probe were inserted into the 3-D printed casing to form the complete device.

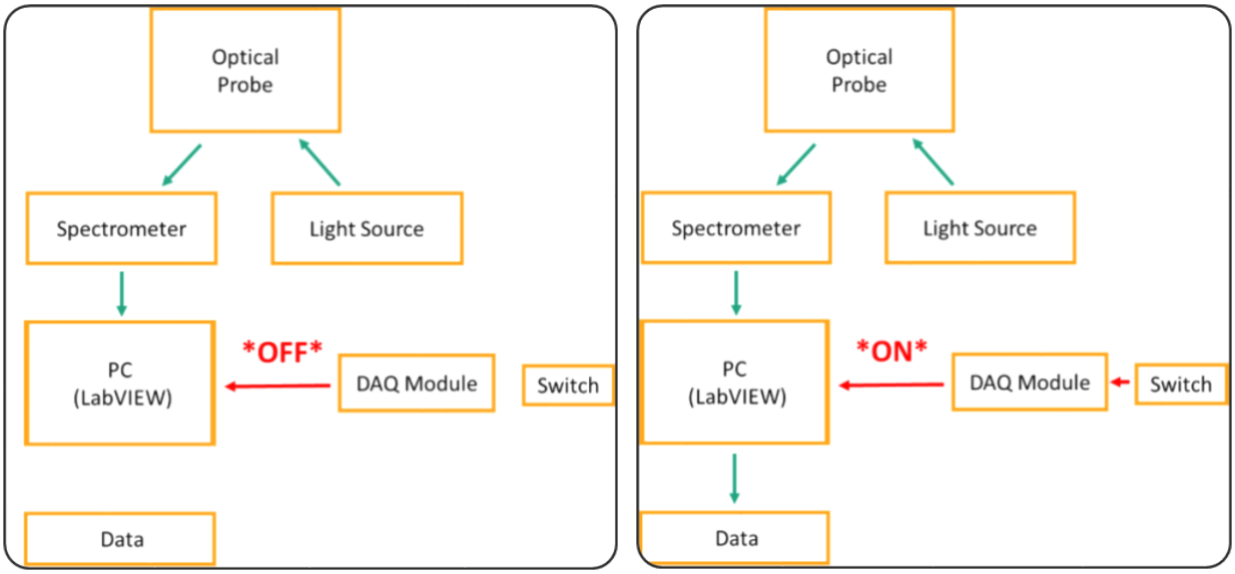

(a) (b)

Figure 29. Flow Diagrams illustrating the data processing of the LRS equipment with the switch and the DAQ module included. (a) Switch in the OFF state, causing the DAQ to send a null signal, preventing the data from being fed into the software. (b) Switch in the ON state, in which by clicking the switch button, the DAQ registers a “yes” signal to the software, which begins to process data.

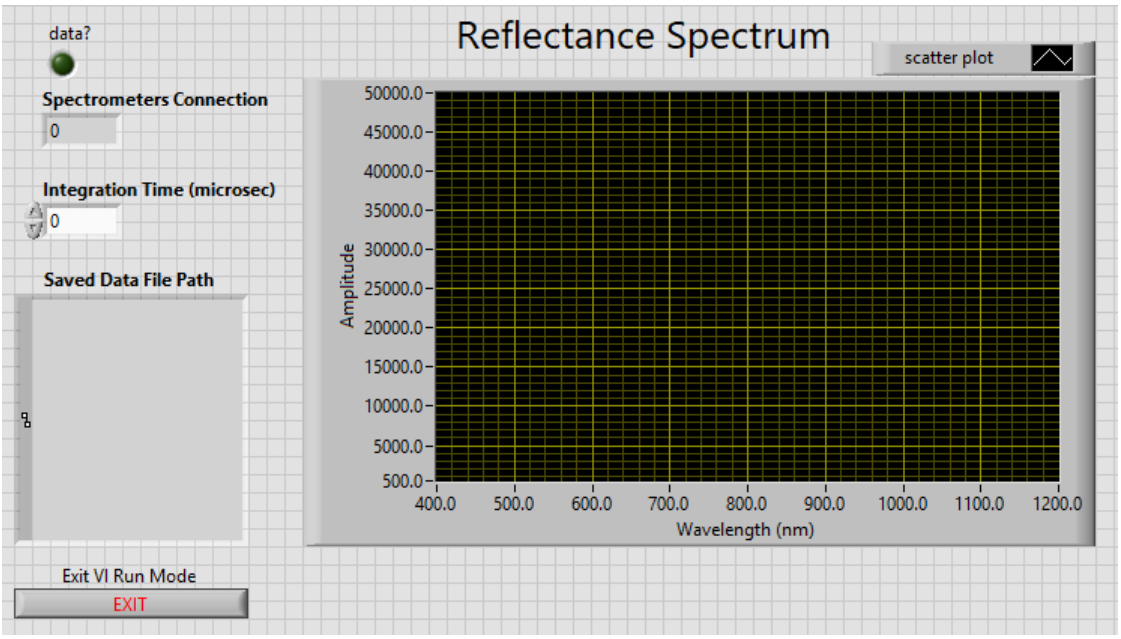

(a)

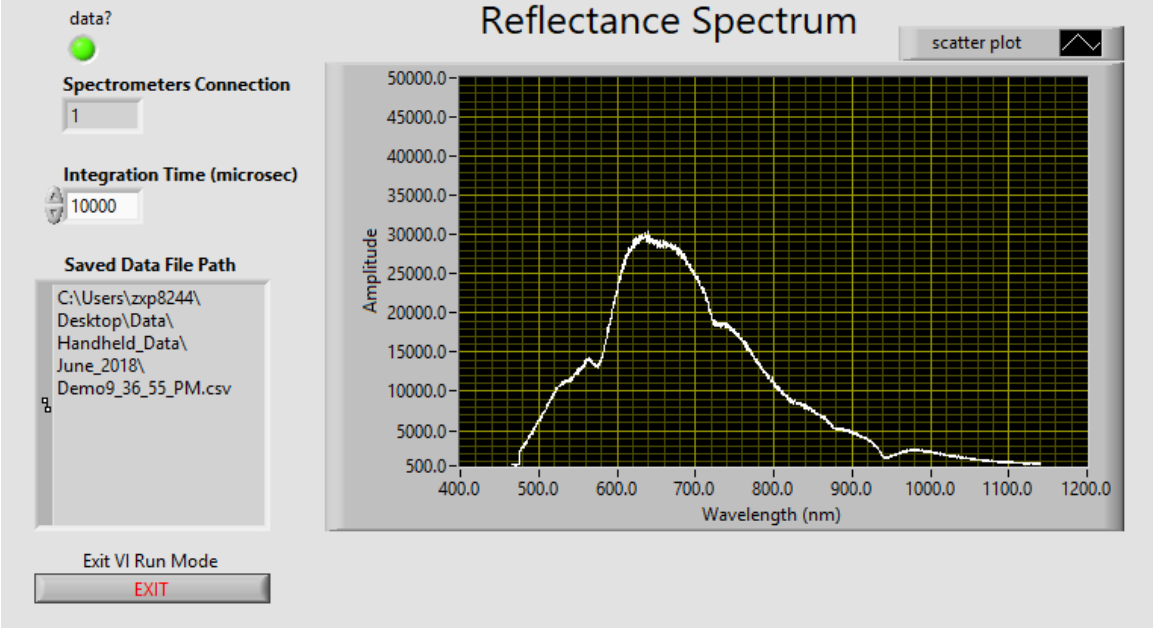

(b)

Figure 30. The newly developed Graphical User Interface (GUI) in LabVIEW, which not only contains the functionality of the original LRS data processing software, OceanView, to stream and save the live LRS spectrum, but it also allows the user to stream and save data on demand via the simple pushes of a tactile switch. (a) The GUI front panel while the system is in OFF mode, where no LRS

data is being sampled. (b) The GUI front panel while in ON mode, which occurs as soon as the user decides to click once or to press and hold the tactile switch. The length of the collected data depends on how long the switch is pressed ON, and the “Integration Time” setting seen as an input slot in the front panel. Integration Time refers to the length of the duration in which the photo sensors are allowed to uptake photons between each discrete data point. Generally, larger the integration time, higher the signal intensity would be. The spectrometer used in this study allows for an integration time range from 1000 to 100000 micro-seconds. Note that smaller the integration time, faster the sampling time will be, which corresponds to more data points saved/second.

In order to bring OceanView’s sophisticated programming into a new data analyzing platform in LabVIEW, all of the necessary drivers used in OceanVIEW were downloaded from the OceanOptic’s website in the pre-packaged form called Omni Driver[42]. Once the OceanView’s original data streaming functionality had been recreated in LabVIEW, then the coding was further customized to be able to begin or end operations based on the digital input conditioning generated by the tactile switch data acquisition module together. The GUI, despite its source codes being sophisticated, was designed to be simple with easy-to-understand options for the user to work with. On the front panel (shown in Figure 30), “Integration Time” and “EXIT” can be interacted with by the user. The “data?” mock LED is an indicator that turns bright green (Figure 30,b) when the tactile switch is activated. The “Spectrometers Connection” displays the value “0” when no spectrometer connection is sensed, and returns “1” when the software detects a spectrometer ready to relay LRS signal to the computer. “Saved Data File Path” outputs the file path of the saved data files, associated with each one is a unique time stamp.

4.3 Device Iteration I

The initial design for the handheld casing primarily focused on the successful accommodation both the tactile switch and the LRS probe while minimizing the size of the finished device.

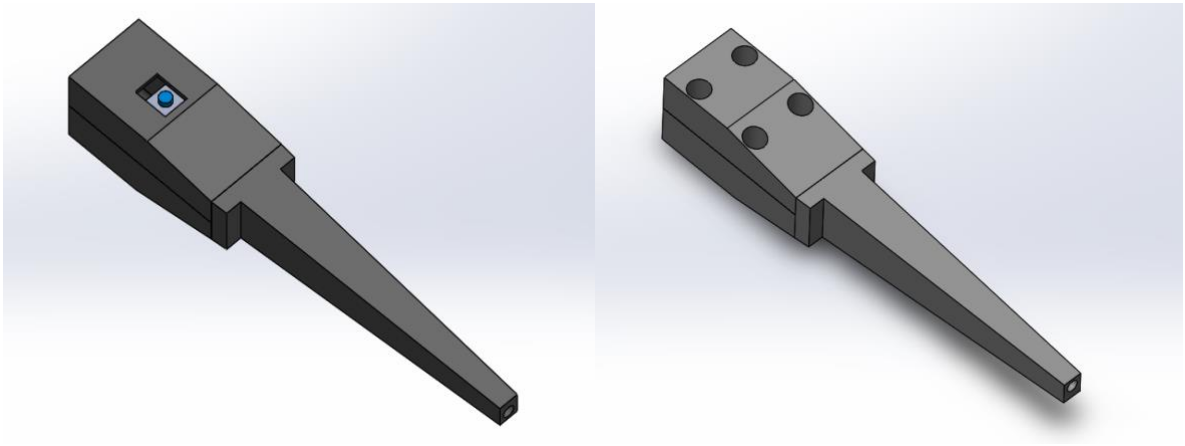

(a) (b)

Figure 31. 3-D renderings (SOLIDWORKS) of the first iteration device. (a) The top side of the device, where the switch will be partially exposed. (b) The back side of the device, where the holes are intended for screws to secure the top and bottom pieces together.

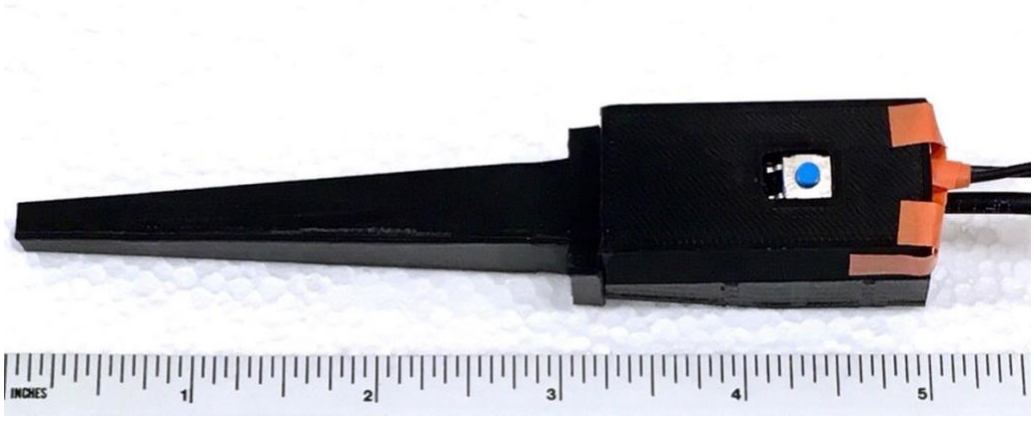

Figure 32. Actual assembled first iteration device.

Although this device was functional, it suffered from a series of shortcomings that caused it to be unstable: 1) The tactile switch was held in place by tape, and even with tapes attached, it shifted constantly during operation, thus causing the copper wires to experience excessive amounts of tear and wear. 2) The LRS probe was not firmly held in place and off-centered (see photograph below). Due to being loosely held, the probe shifted and led to inconsistent readings even if the device was pointed at the same position on a sample repeatedly. 3) The length of the sleeve was too long, creating a retraction distance of greater than 1mm.

Figure 33. The front view of the actual device. As seen in the photograph, the optical probe is not centered with respect to the center of the casing.

4.4 Device Iteration II

In the follow up version of the handheld device, all of the previously addressed issued were fixed with new design elements. While the overall form factor remained nearly identical, the finished product contains numerous nuances that allowed it greatly improved stability and durability.

(a)

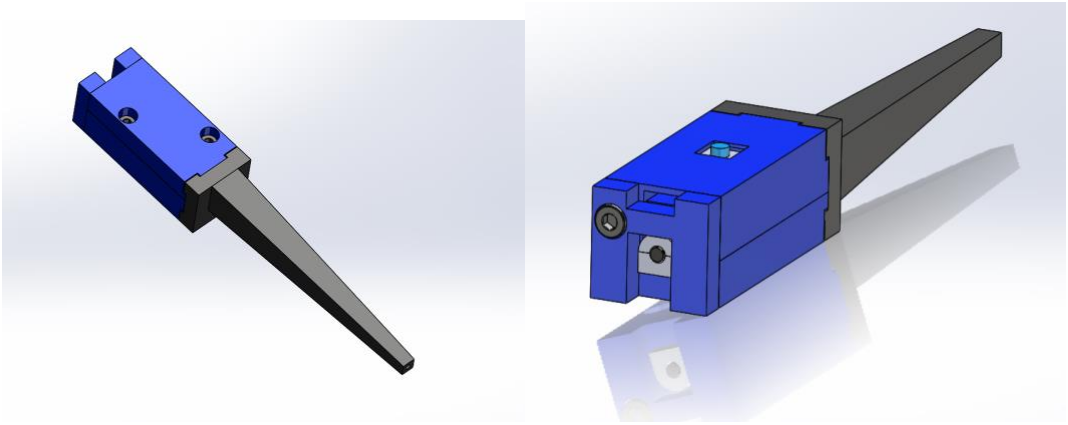

(b) (c)

Figure 34. 3-D renderings of the improved design. (a) The top side, where it can be seen that the black sleeve portion is secured by a screw and is therefore detachable in lieu of further modifications. (b) The bottom side reveals reduced number of screws. (c) The back end view illustrates the addition of screwed-on cap, which serves to keep the internals firmly in place.

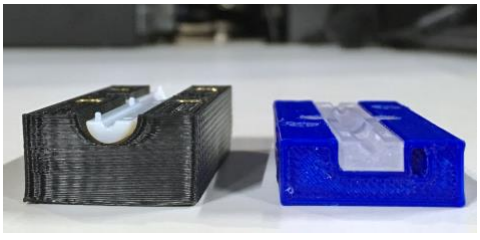

(a) (b)

Figure 35. Partial cross-section view of the old and new casings, both revealing a bi-half of the internal sleeve that wraps around the small dimensions around the needle probe (a) In the first

iteration, the internal sleeve was cylindrical, with much smaller diameter than its designated groove, which resulted in the optical probe to shift and rotate (b) In the follow-up iteration, the internal sleeve's geometry was partially changed to rectangular. This alteration acted as an effective solution to the probe's rotation issue.

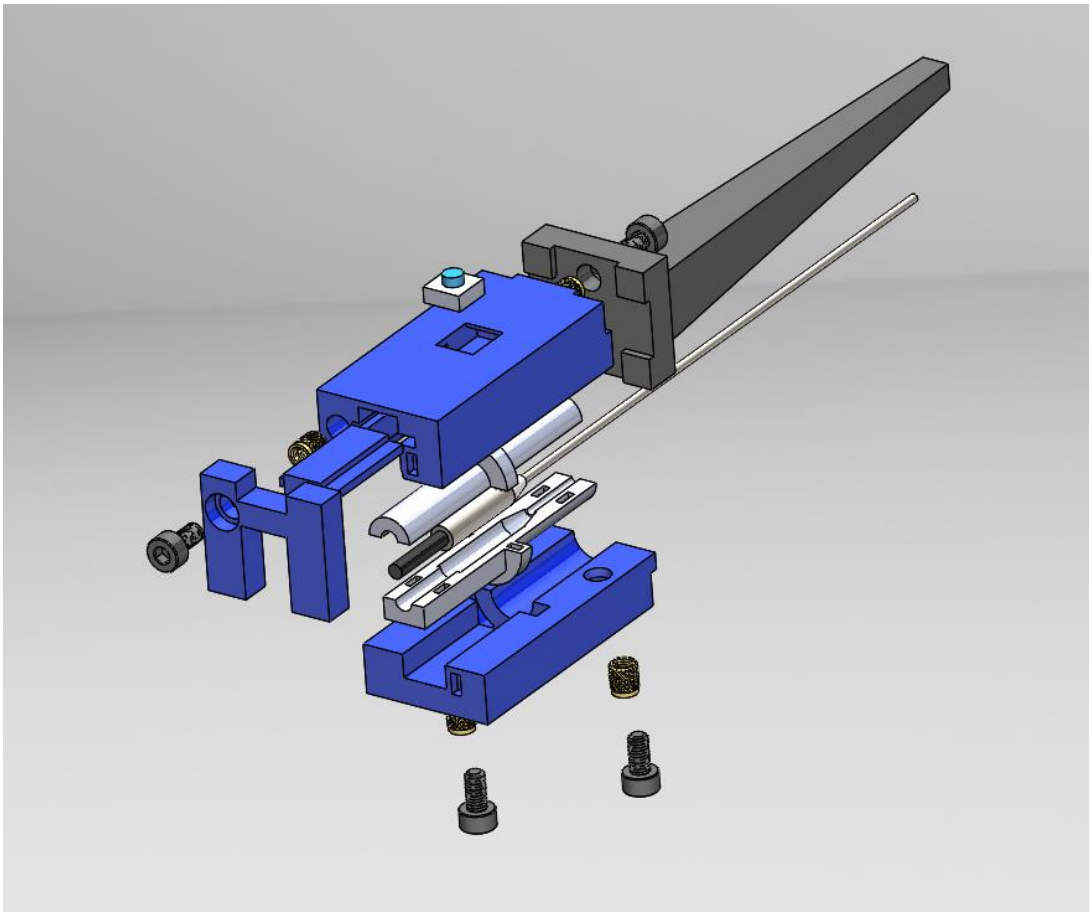

Figure 36. Exploded view of the improved design. All of the components are shown, including the screws and the push-to-expand brass insert grooves for the screws to fit in. Contrary to the old design, the new device is more compartmentalized, and relies on little to no use of adhesives.

Chapter 5: Discussion

5.1 Sleeve Experiments: Initial and Diameter Testing

The results from the first set of sleeve experiments returned negative results on the expected shielding capacity of an external casing. While slightly reduced noise spikes were observed in the sleeve group's spectra, their overall signal was too contaminated to prove useful. Furthermore, the results suggest no improvements in shielding with the inclusion of larger sleeve cavities.

The aforementioned observations offer different explanation of how environmental noise is generated. Previously, it was long thought that the noise was as result of ambient light escaping into the small gap at the interface between the probe tip and the tissue, and therefore allowing the probe sensor to pick up additional scattering. It was this initial hypothesis that led to the proposal of using sleeve casing, whose main objective was to reduce noise by covering the tip of the probe. However, new evidence from this study point to a different explanation of noise occurrence, which results from ambient light penetrating and propagating the entire tissue area outside the coverage of the sleeve. This new hypothesis changes the how the problem of noise reduction should be approached. Whereas the previous focus was placed upon shielding the tip of the probe, or more specifically, the detector fiber, now it will also include the need to prevent the entire tissue sample from being exposed to the ambient light.

The newly formed hypothesis was reinforced by the sleeve diameter experiments, where sleeves covering significantly larger areas (most significantly the 16.8mm group) demonstrated fewer and less intense noise artifacts in their spectra. Overall, the experiment illustrated a positively linear relationship between tissue coverage and noise reduction. However, from the perspective of design and functionality, it would be unrealistic to incorporate a sleeve with large diameters, as it would impede the user's ability to aim and specifically pinpoint the probe on specific areas along the tissue, especially when the area of suspicion is very small. Therefore, with this design consideration in mind, it would be ideal to equip the handheld device with a small diameter sleeve, if any, and overcome the problem of noise shielding through additional measures.

5.2 Sleeve Experiments: Light Conditions

Based on the new understanding of how noise is generated in the LRS signal (discussed in section above), a new solution to eliminate noise was conceptualized: direct manipulation of the environmental lighting, the source of noise in LRS spectra. As a result of this investigation, it was surprisingly discovered that once the surrounding light is dimmed by 50%, almost all noise was eliminated regardless of the probe was openly exposed or shielded by the sleeve. From this finding, it can be argued that in order to replace the gold standard box shielding, one could simply dim the lights in the room, or use a small lamp at a proper distance to provide room lighting during LRS

measurement. It can be further argued that there may not be a need to utilize any sleeve shielding in the final device design at all.

5.3 Sleeve Experiments: Retraction Depth

Former studies on the LRS imaging method have pointed out that applied pressure is a factor that significantly influences the LRS signal[39,40], and while in the handheld configuration, the effect of variable pressure upon the LRS signal would become more significant. As such, setting significant retraction depths and preventing direct contact between the probe and the sample was a provisional attempt at overcoming the challenge of inconsistent pressure application from human handling. It was thought that once the probe is held back from pushing down upon the tissue, the signal variation from constantly shifting pressure would be reduced.

Contrary to the expected outcome, it was seen from the retraction distance experiments that whether or not the probe made contact with the sample had no significant effect on how much the LRS readings varied as it was handheld. At a glance, based on the intensity and deviation magnitudes in Figure 25, it may appear that by not allowing the probe to make tissue contact, the signal variations actually increased. But upon closer examination, if each retraction distance group's average spectrum was divided by the magnitude of its own deviation, it will be seen that there exists a nearly 50% variation in all three groups' signals. From this, it is concluded that retraction distance cannot act as

the solution to compensate for the significant pressure variation in the handheld LRS device.

5.4 Old and New Probe Comparison

Despite having identical 200-micron source and detector fibers and the same fiber separation distance, there are exists differences in unspecified physical attributes of both probes that causes their yielded spectra to be slightly different in intensity, where the new probe returns intensity values that are slightly lower. However, the slightly lower intensity seen in the new probe could be attributed to inconsistencies in the white sample calibration measures, for the intensity difference is not observed in the raw data prior to normalization. To confirm this, the white sample measurements will be to be repeated with improved protocol that ensures both the new and old probes are measuring at the exact same locations on the white calibration sample.

Even if the slight intensity difference persists, it can be accounted for by determining a multiplication factor to adjust the difference between the two probes. More significantly both the new an old probes demonstrate nearly identical slopes and intensities in the 750 to 850 nm region. Through cross-referencing algorithm exercises, previous studies were able to narrow down the range from 700 nm to 850 nm as being the region most specific towards differentiating prostate cancer tissues[27]. Therefore, the new probe is considered viable for future measurements on prostate specimens, so long as the 750 to 850 nm region is the feature being referenced to the old probe's data bank.

5.5 Sleeve Experiments: Device Design

After arriving to the second official iteration, the device has reached a stage where it can consistently perform without failing or displaying mechanical inconsistencies. Since the development of the device ran parallel to the experimental steps in this study, certain experimental conclusions were not able to be reflected into the device design. For instance, although it was seen that the usage of the sleeve provided no significant shielding properties, the 3-D printed device still included a sleeve covering the full length of the probe body, when ideally, based on the experiment findings, the sleeve could be altered to partially cover the probe for physical protection, leaving the tip of the probe entirely exposed.

Conclusions

In this research effort to improve the LRS imaging modality towards positive surgical margin detection in prostate cancer, the most significant discoveries and achievements are as follows:

1) Noises in the LRS signal originate from the surrounding light propagating throughout the tissue sample, and not from light escaping into the gap at the interface of the probe tip and the tissue surface. And by simply encasing the tip of the optical probe in a sleeve shied cannot yield noise free signals.
2) Under dimmed light conditions, the noise artifacts in the LRS signal is almost entirely removed, even when the probe is without any shielding, indicating that a totally dark environment is not needed for accurate measurements, and that the need for the box shielding is not critical.
3) The successful development of a handheld LRS device, which can collect data by the simple push of its tactile switch.

In conclusion, this study serves as a first step towards researching and developing the LRS imaging modality into a more effective tool. Further studies should place emphasis on investigating methods of reducing the signal variability as a result of human error when the LRS probe is being handheld. Despite the use of a sleeve shielding at the tip of the probe was not proven to be significantly effective in noise blocking, it can instead be utilized for purposes of reducing human error. The figure below demonstrates how

the concept of a retractable sleeve can be used to keep the hand-applied pressure more consistent during data collection.

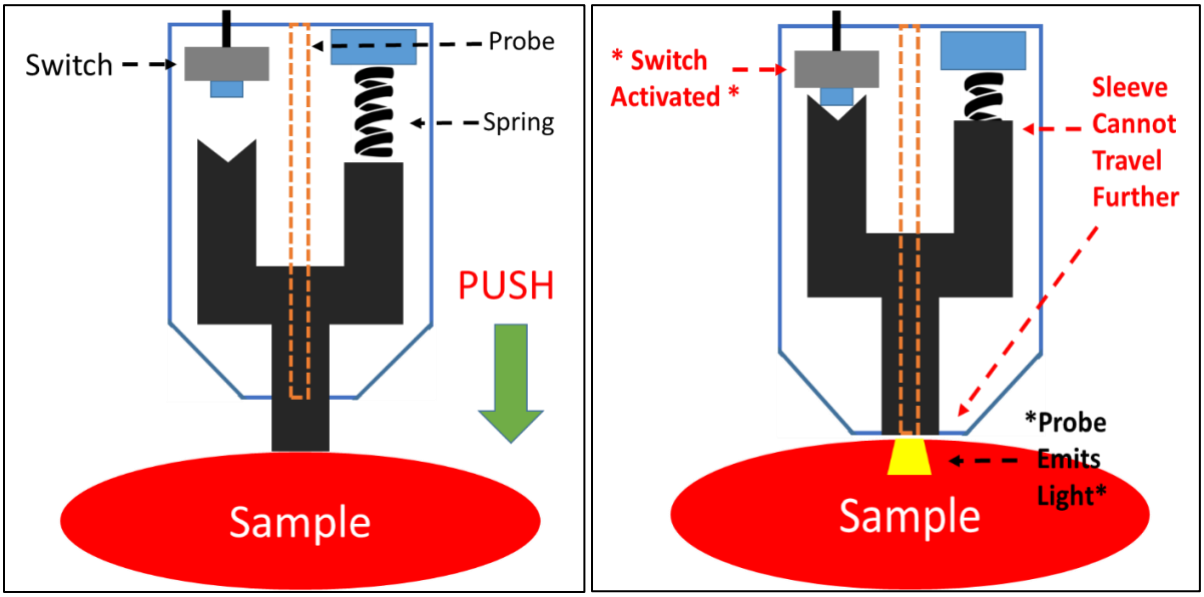

(a) (b)

Figure 37. An illustration of a retractable sleeve mechanism, which slides back into the handheld casing to activate the data-acquisition switch. The previously hand activated switch could now be engaged only when a fixed threshold pressure, depending on the internal spring deployed, has been applied to the tip of the sleeve, which retracts just far enough for the LRS probe to make contact with the sample. Note that only this figure only displays tip of the device concept, where the new retractable sleeve will be installed. (a) The sleeve (black) held at its resting position by a spring inside the casing. In order to lower the device to meet the sample, the user will push down on the device to retract the sleeve. (b) The sleeve at its stopping position, where the sleeve's left moving arm has retracted just far enough to activate the switch inside, which signals the software to save data. This mechanism can better ensure that each data point, or snap shot taken of the live LRS spectrum, is taken at the precise moment when a fixed amount of pressure was applied in order to engage the switch, which takes away the previously challenging presence of human error due to the exact amount of pressure cannot be accurately gauged for the collection of each data point.

References:

1. Kufe, D., Holland, J., & Frei, E. (2006). *Holland-Frei cancer medicine 7*. Hamilton, Ont.: BC Decker.
2. W.A. Schulz, M. Burchardt, M.V. Cronauer; Molecular biology of prostate cancer, MHR: Basic science of reproductive medicine, Volume 9, Issue 8, 1 August 2003, Pages 437–448
3. Borchert, A., & Leavitt, D. A. (2018). A Review of Male Sexual Health and Dysfunction Following Surgical Treatment for Benign Prostatic Hyperplasia and Lower Urinary Tract Symptoms. *Current Urology Reports*, *19*(8), 66.
4. Lin, P. H., Aronson, W., & Freedland, S. J. (2017, November). An update of research evidence on nutrition and prostate cancer. In *Urologic Oncology: Seminars and Original Investigations*. Elsevier.
5. Griend, D., Vogelzang, N., & Lee, R. (2018). Molecular Biology of Prostate Cancer. Retrieved from https://www.uptodate.com/contents/molecular-biology-of-prostate-cancer
6. Lei, J. H., Liu, L. R., Wei, Q., Song, T. R., Yang, L., Meng, Y., & Han, P. (2016). Androgen-deprivation therapy alone versus combined with radiation therapy or chemotherapy for nonlocalized prostate cancer: a systematic review and meta-analysis. *Asian journal of andrology*, *18*(1), 102
7. Salinas, C. A., Tsodikov, A., Ishak-Howard, M., & Cooney, K. A. (2014). Prostate cancer in young men: an important clinical entity. *Nature Reviews Urology*, *11*(6), 317.
8. Peisch, S. F., Van Blarigan, E. L., Chan, J. M., Stampfer, M. J., & Kenfield, S. A. (2017). Prostate cancer progression and mortality: a review of diet and lifestyle factors. *World journal of urology*, *35*(6), 867-874.
9. Cao, Y., & Ma, J. (2011). Body-mass index, prostate cancer-specific mortality and biochemical recurrence: a systematic review and meta-analysis. *Cancer prevention research*, canprevres-0229.
10. Kenfield, S. A., Stampfer, M. J., Chan, J. M., & Giovannucci, E. (2011). Smoking and prostate cancer survival and recurrence. *Jama*, *305*(24), 2548-2555.
11. Chang, S. N., Han, J., Abdelkader, T. S., Kim, T. H., Lee, J. M., Song, J., ... & Park, J. H. (2014). High animal fat intake enhances prostate cancer progression and reduces glutathione peroxidase 3 expression in early stages of TRAMP mice. *The Prostate*, *74*(13), 1266-1277.
12. Liang, P., Henning, S. M., Schokrpur, S., Wu, L., Doan, N., Said, J., ... & Aronson, W. J. (2016). Effect of Dietary Omega-3 Fatty Acids on Tumor-Associated Macrophages and Prostate Cancer Progression. *The Prostate*, *76*(14), 1293-1302.
13. Delongchamps, N. B., & Haas, G. P. (2009). Saturation biopsies for prostate cancer: current uses and future prospects. *Nature Reviews Urology*, *6*(12), 645.
14. Rocco, B., de Cobelli, O., Leon, M. E., Ferruti, M., Mastropasqua, M. G., Matei, D. V., ... & Djavan, B. (2006). Sensitivity and detection rate of a 12-core trans-perineal prostate biopsy: preliminary report. *European urology*, *49*(5), 827-833.
15. Gleason, D. F., Mellinger, G. T., Arduino, L. J., Bailar III, J. C., Becker III, L. E., Berman III, H. I., ... & Elliot, J. S. (1974). Prediction of prognosis for prostatic

adenocarcinoma by combined histological grading and clinical staging. *The Journal of urology*, *111*(1), 58-64.
16. Roberts, M. J., Teloken, P., Chambers, S. K., Williams, S. G., Yaxley, J., Samaratunga, H., & Frydenberg, M. (2018). Prostate Cancer Detection. In *Endotext [Internet]*. MDText. com, Inc..
17. Heidenreich, A., Aus, G., Bolla, M., Joniau, S., Matveev, V. B., Schmid, H. P., & Zattoni, F. (2008). EAU guidelines on prostate cancer. *European urology*, *53*(1), 68-80.
18. Catalona, W. J., Smith, D. S., Ratliff, T. L., & Basler, J. W. (1993). Detection of organ-confined prostate cancer is increased through prostate-specific antigen—based screening. *Jama*, *270*(8), 948-954.
19. Crawford, E. D., DeAntoni, E. P., Etzioni, R., Schaefer, V. C., Olson, R. M., & Ross, C. A. (1996). Serum prostate-specific antigen and digital rectal examination for early detection of prostate cancer in a national community-based program. *Urology*, *47*(6), 863-869.
20. Mettlin, C., Jones, G., Averette, H., Gusberg, S. B., & Murphy, G. P. (1993). Defining and updating the American Cancer Society guidelines for the cancer-related checkup: prostate and endometrial cancers. *CA: a cancer journal for clinicians*, *43*(1), 42-46.
21. Thompson, I. M., Pauler, D. K., Goodman, P. J., Tangen, C. M., Lucia, M. S., Parnes, H. L., ... & Crowley, J. J. (2004). Prevalence of prostate cancer among men with a prostate-specific antigen level≤ 4.0 ng per milliliter. *New England Journal of Medicine*, *350*(22), 2239-2246.
22. Hoffman, A., & Half, E. E. (2017). Update on Screening for Urological Malignancies. *Rambam Maimonides medical journal*, *8*(4).
23. Filella, X., & Giménez, N. (2013). Evaluation of [−2] proPSA and Prostate Health Index (phi) for the detection of prostate cancer: a systematic review and meta-analysis. *Clinical chemistry and laboratory medicine*, *51*(4), 729-739.
24. Parekh, D. J., Punnen, S., Sjoberg, D. D., Asroff, S. W., Bailen, J. L., Cochran, J. S., ... & Gambla, M. (2015). A multi-institutional prospective trial in the USA confirms that the 4Kscore accurately identifies men with high-grade prostate cancer. *European urology*, *68*(3), 464-470.
25. Mohler, J. L., Armstrong, A. J., Bahnson, R. R., D'Amico, A. V., Davis, B. J., Eastham, J. A., ... & Hurwitz, M. (2016). Prostate cancer, version 1.2016. *Journal of the National Comprehensive Cancer Network*, *14*(1), 19-30.
26. Fuller, C. D., Dang, N. D., Wang, S. J., Desai, P., Choi, M., Thomas Jr, C. R., & Fuss, M. (2009). Image-guided intensity-modulated radiotherapy (IG-IMRT) for biliary adenocarcinomas: Initial clinical results. *Radiotherapy and Oncology*, *92*(2), 249-254.
27. Morgan, M. S., Lay, A. H., Wang, X., Kapur, P., Ozayar, A., Sayah, M., ... & Cadeddu, J. A. (2016). Light reflectance spectroscopy to detect positive surgical margins on prostate cancer specimens. *The Journal of urology*, *195*(2), 479-484.
28. Tan, L., Wang, L. L., Ranasinghe, W., Persad, R., Bolton, D., Lawrentschuk, N., & Sengupta, S. (2018). Survival outcomes of younger men (< 55 years) undergoing radical prostatectomy. *Prostate international*, *6*(1), 31-35.

29. Lee, J., Lee, S., & Bae, Y. (2012). Multiple margin positivity of frozen section is an independent risk factor for local recurrence in breast-conserving surgery. *Journal of breast cancer*, *15*(4), 420-426.
30. Orosco, R. K., Tapia, V. J., Califano, J. A., Clary, B., Cohen, E. E., Kane, C., ... & Pang, J. (2018). Positive Surgical Margins in the 10 Most Common Solid Cancers. *Scientific reports*, *8*(1), 5686.
31. Yossepowitch, O., Bjartell, A., Eastham, J. A., Graefen, M., Guillonneau, B. D., Karakiewicz, P. I., ... & Montorsi, F. (2009). Positive surgical margins in radical prostatectomy: outlining the problem and its long-term consequences. *European urology*, *55*(1), 87-99.
32. Ritch, C. R., You, C., May, A. T., Herrell, S. D., Clark, P. E., Penson, D. F., ... & Barocas, D. A. (2014). Biochemical recurrence–free survival after robotic-assisted laparoscopic vs open radical prostatectomy for intermediate-and high-risk prostate cancer. *Urology*, *83*(6), 1309-1315.
33. Lue, N., Kang, J. W., Yu, C. C., Barman, I., Dingari, N. C., Feld, M. S., ... & Fitzmaurice, M. (2012). Portable optical fiber probe-based spectroscopic scanner for rapid cancer diagnosis: a new tool for intraoperative margin assessment. *PloS one*, *7*(1), e30887.
34. Novikova, T. (2017). Optical techniques for cervical neoplasia detection. *Beilstein journal of nanotechnology*, *8*, 1844.
35. Giller, C. A., Liu, H., German, D. C., Kashyap, D., & Dewey Jr, R. B. (2009). A stereotactic near-infrared probe for localization during functional neurosurgical procedures: further experience. *Journal of neurosurgery*, *110*(2), 263-273.
36. Sharma, V., Olweny, E. O., Kapur, P., Cadeddu, J. A., Roehrborn, C. G., & Liu, H. (2014). Prostate cancer detection using combined auto-fluorescence and light reflectance spectroscopy: ex vivo study of human prostates. *Biomedical optics express*, *5*(5), 1512-1529.
37. Lay, A. H., Wang, X., Morgan, M. S., Kapur, P., Liu, H., Roehrborn, C. G., & Cadeddu, J. A. (2016). Detecting positive surgical margins: utilisation of light-reflectance spectroscopy on ex vivo prostate specimens. *BJU international*, *118*(6), 885-889
38. Zonios, G., & Dimou, A. (2006). Modeling diffuse reflectance from semi-infinite turbid media: application to the study of skin optical properties. *Optics express*, *14*(19), 8661-8674.
39. Chan, Henry. “Light Reflectance Spectroscopy for the Detection of Positive Surgical Margin of Prostate Cancer.” *The University of Texas at Arlington, Master’s Dissertation* (2017).
40. Sharma, Vikrant. “A Novel Minimally Invasice Dual-Modality Fiber Optic Probe For Prostate Cancer Detection.” *The University of Texas at Arlington, PhD Dissertation* (2012).
41. Sircan-Kucuksayan, A., Uyuklu, M., & Canpolat, M. (2015). Diffuse reflectance spectroscopy for the measurement of tissue oxygen saturation. *Physiological measurement*, *36*(12), 2461.
42. Ocean Optics. (2018). *OCEANOPTICS*. [online] Available at: https://oceanoptics.com/ [Accessed 9 Aug. 2018].

Appendix A

Official SolidWorks® Drawings of Finalized Device Components

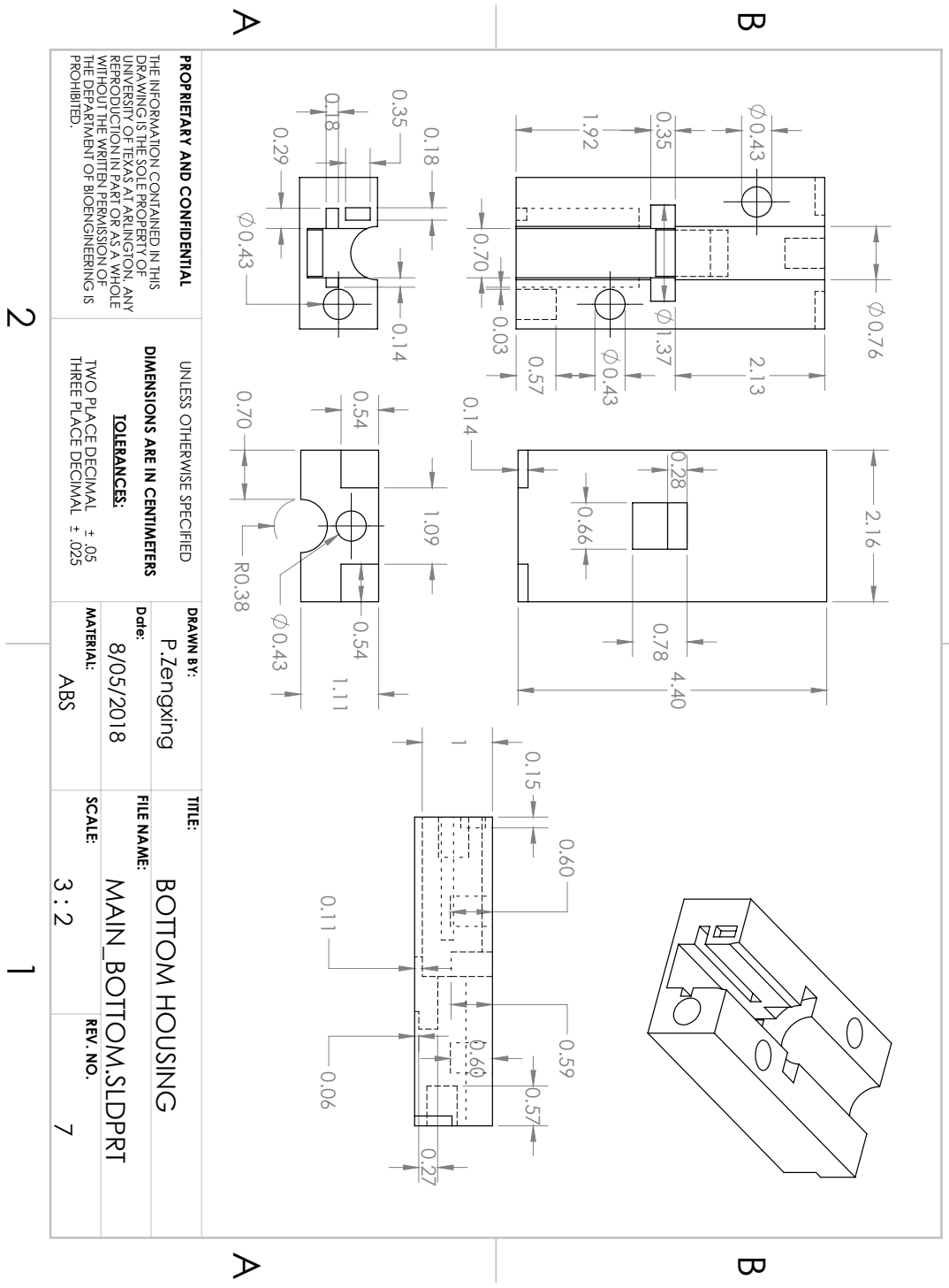

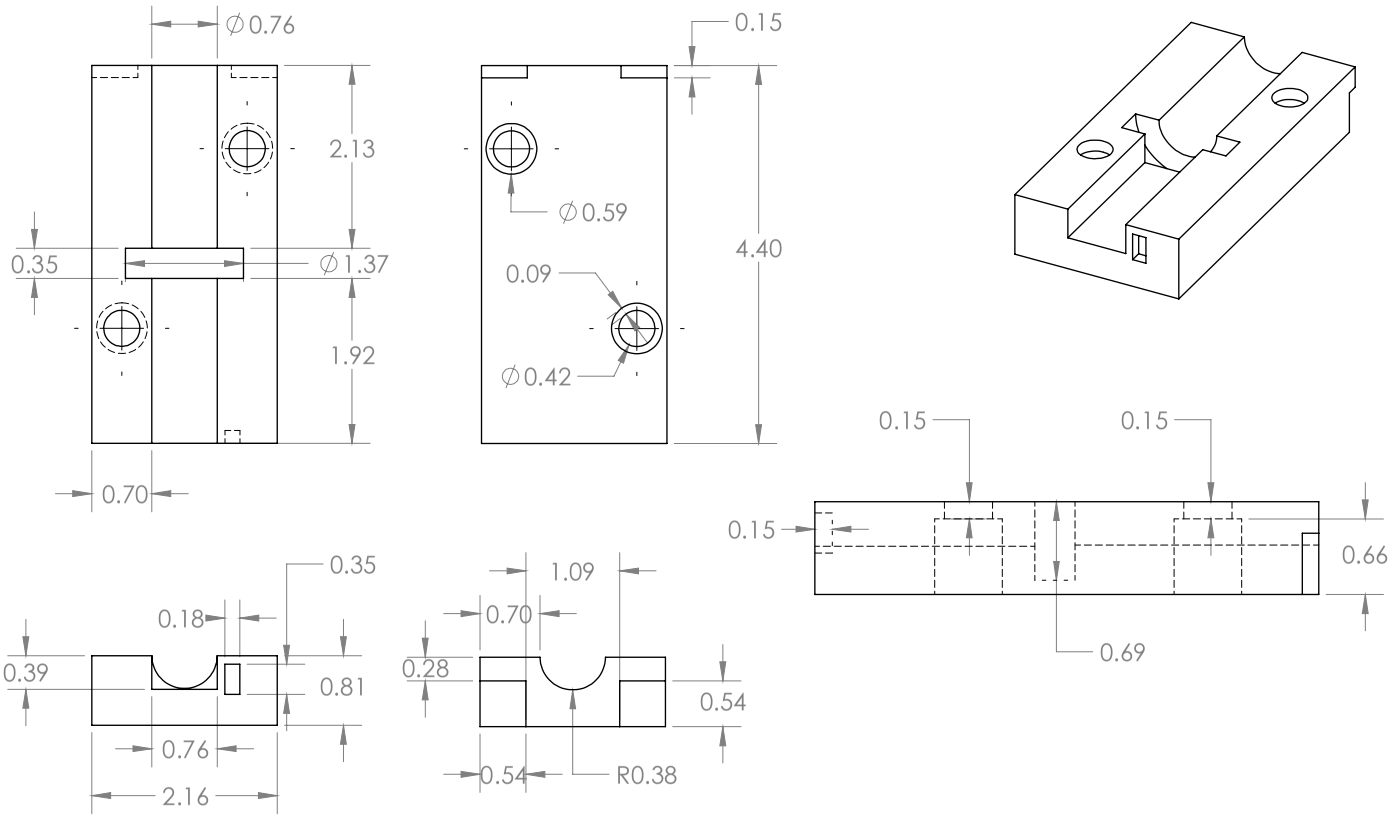

PROPRIETARY AND CONFIDENTIAL THE INFORMATION CONTAINED IN THIS DRAWING IS THE SOLE PROPERTY OF UNIVERSITY OF TEXAS AT ARLINGTON. ANY REPRODUCTION IN PART OR AS A WHOLE WITHOUT THE WRITTEN PERMISSION OF THE DEPARTMENT OF BIOENGINEERING IS PROHIBITED.	UNLESS OTHERWISE SPECIFIED **DIMENSIONS ARE IN CENTIMETERS** **TOLERANCES:** TWO PLACE DECIMAL ± .05 THREE PLACE DECIMAL ± .025	**DRAWN BY:** P.Zengxing **Date:** 8/05/2018 **MATERIAL:** ABS	**TITLE:** TOP HOUSING **FILE NAME:** MAIN_TOP.SLDPRT **SCALE:** 3 : 2	**REV. NO.** 7

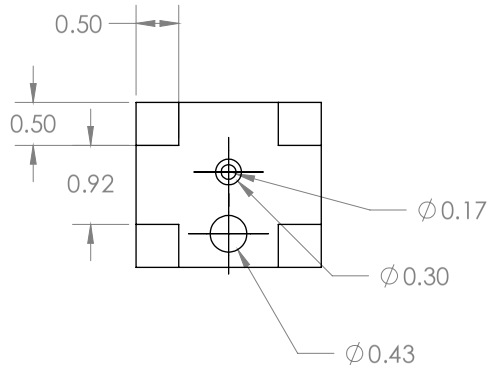

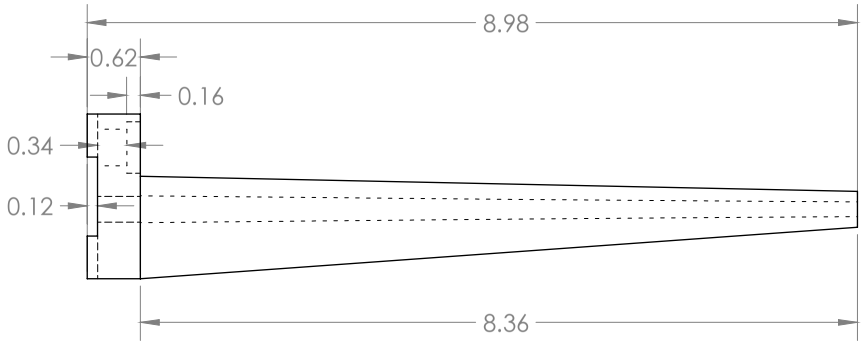

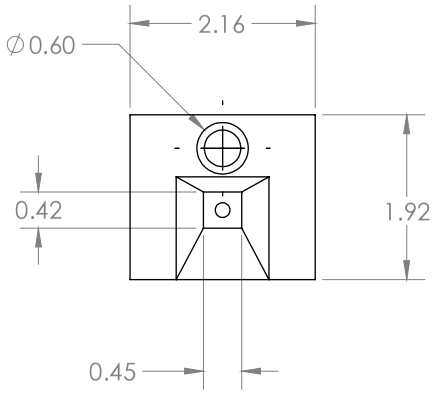

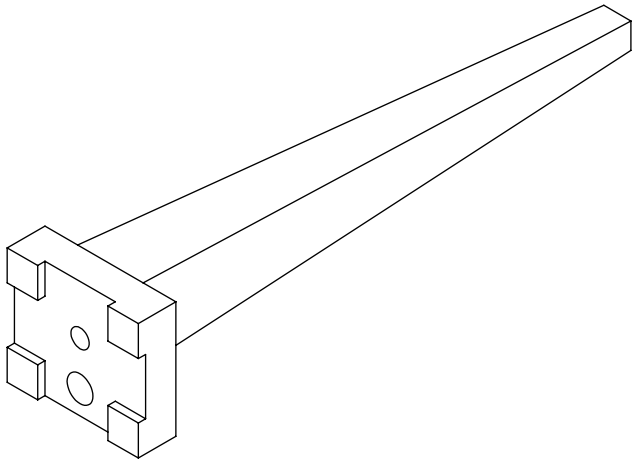

PROPRIETARY AND CONFIDENTIAL THE INFORMATION CONTAINED IN THIS DRAWING IS THE SOLE PROPERTY OF UNIVERSITY OF TEXAS AT ARLINGTON. ANY REPRODUCTION IN PART OR AS A WHOLE WITHOUT THE WRITTEN PERMISSION OF THE DEPARTMENT OF BIOENGINEERING IS PROHIBITED.	UNLESS OTHERWISE SPECIFIED **DIMENSIONS ARE IN CENTIMETERS** **TOLERANCES:** TWO PLACE DECIMAL ± .05 THREE PLACE DECIMAL ± .025	**DRAWN BY:** P.Zengxing **Date:** 8/05/2018 **MATERIAL:** ABS	**TITLE:** PROBE SHIELDING **FILE NAME:** SLEEVE_SHIELDING.SLDPRT **SCALE:** 3 : 2	**REV. NO.** 3

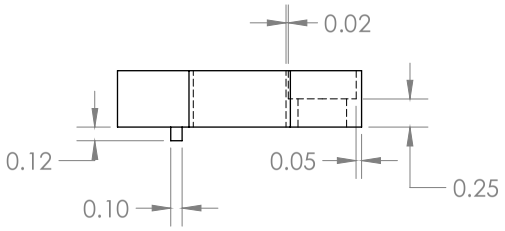

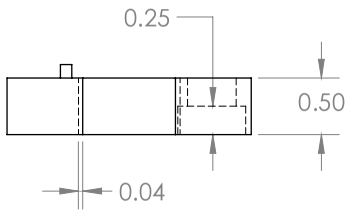

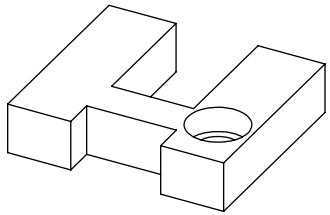

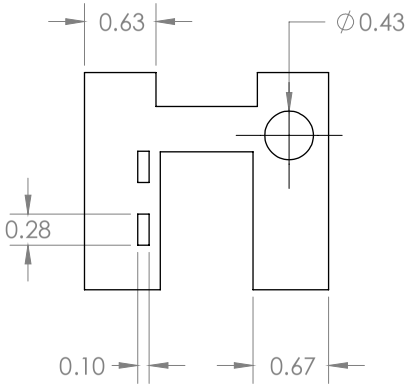

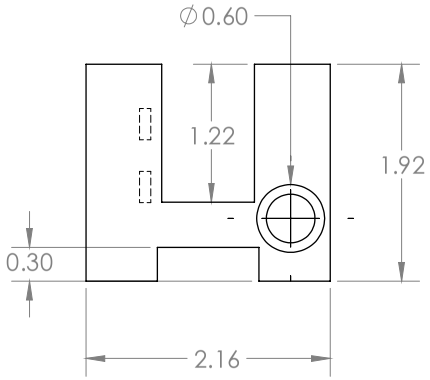

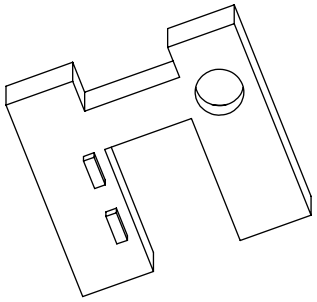

PROPRIETARY AND CONFIDENTIAL THE INFORMATION CONTAINED IN THIS DRAWING IS THE SOLE PROPERTY OF UNIVERSITY OF TEXAS AT ARLINGTON. ANY REPRODUCTION IN PART OR AS A WHOLE WITHOUT THE WRITTEN PERMISSION OF THE DEPARTMENT OF BIOENGINEERING IS PROHIBITED.	UNLESS OTHERWISE SPECIFIED **DIMENSIONS ARE IN CENTIMETERS** **TOLERANCES:** TWO PLACE DECIMAL ± .05 THREE PLACE DECIMAL ± .025	**DRAWN BY:** P.Zengxing **Date:** 8/05/2018 **MATERIAL:** ABS	**TITLE:** REAR CAP **FILE NAME:** REAR_CAP.SLDPRT **SCALE:** 2 : 1	**REV. NO.** 3

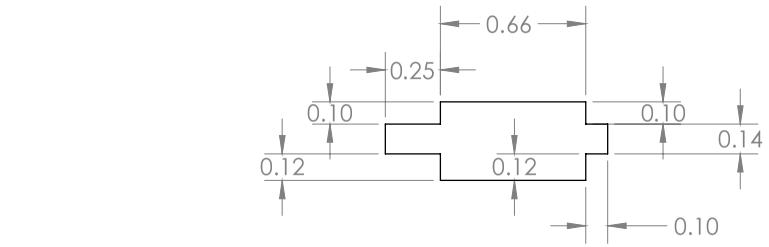

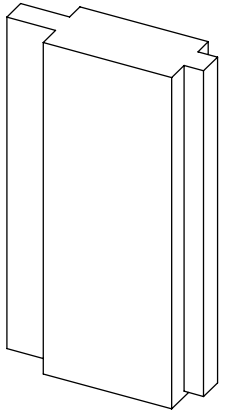

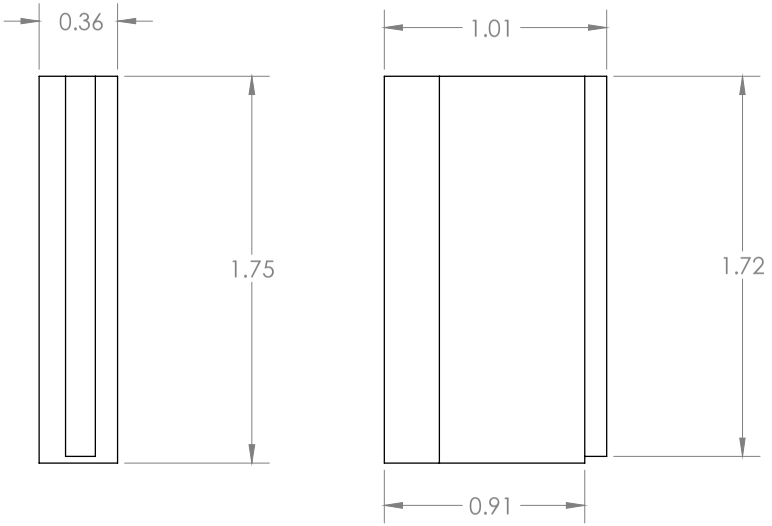

PROPRIETARY AND CONFIDENTIAL THE INFORMATION CONTAINED IN THIS DRAWING IS THE SOLE PROPERTY OF UNIVERSITY OF TEXAS AT ARLINGTON. ANY REPRODUCTION IN PART OR AS A WHOLE WITHOUT THE WRITTEN PERMISSION OF THE DEPARTMENT OF BIOENGINEERING IS PROHIBITED.	UNLESS OTHERWISE SPECIFIED **DIMENSIONS ARE IN CENTIMETERS** **TOLERANCES:** TWO PLACE DECIMAL ± .05 THREE PLACE DECIMAL ± .025	**DRAWN BY:** P.Zengxing **Date:** 8/05/2018 **MATERIAL:** ABS	**TITLE:** HOUSING INSERT **FILE NAME:** SPACER_INSERT.SLDPRT **SCALE:** 4 : 1	**REV. NO.** 3

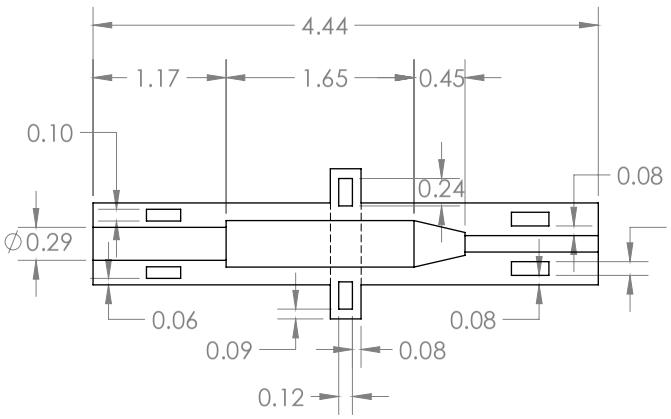

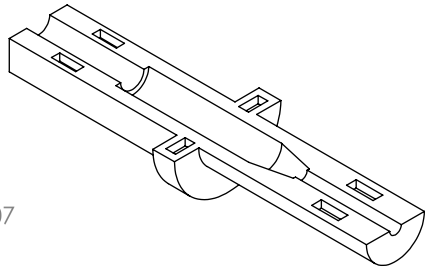

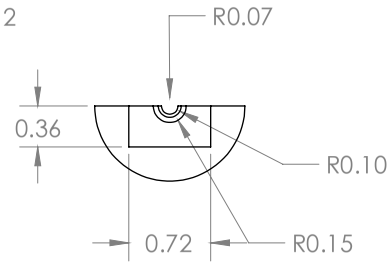

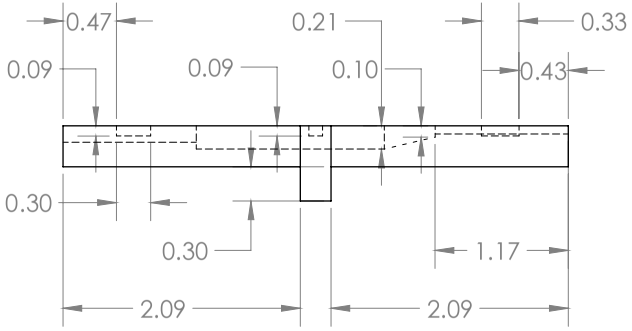

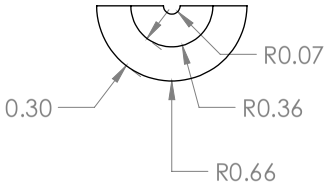

PROPRIETARY AND CONFIDENTIAL THE INFORMATION CONTAINED IN THIS DRAWING IS THE SOLE PROPERTY OF UNIVERSITY OF TEXAS AT ARLINGTON. ANY REPRODUCTION IN PART OR AS A WHOLE WITHOUT THE WRITTEN PERMISSION OF THE DEPARTMENT OF BIOENGINEERING IS PROHIBITED.	UNLESS OTHERWISE SPECIFIED **DIMENSIONS ARE IN CENTIMETERS** **TOLERANCES:** TWO PLACE DECIMAL ± .05 THREE PLACE DECIMAL ± .025	**DRAWN BY:** P.Zengxing	**TITLE:** BOTTOM INTERNAL SHEATH	
		Date: 8/05/2018	**FILE NAME:** PROBE_SHEATH_1.SLDPRT	
		MATERIAL: SLA RESIN	**SCALE:** 2 : 1	**REV. NO.** 5

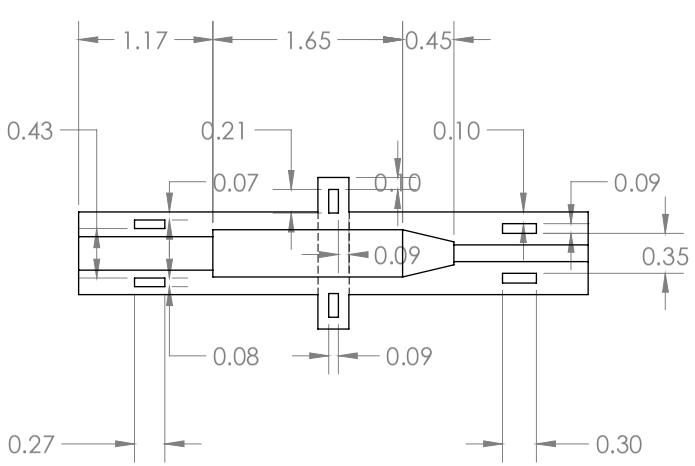

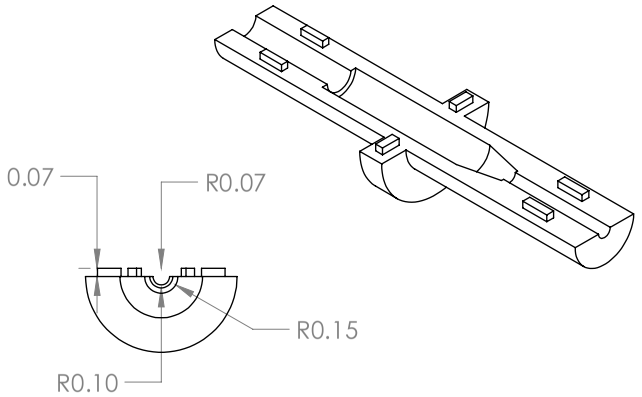

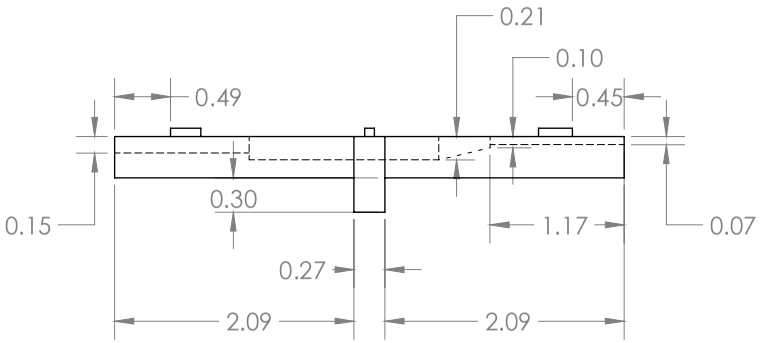

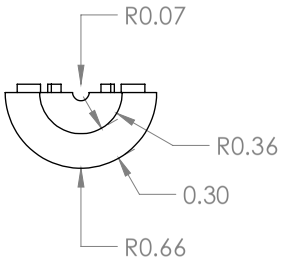

PROPRIETARY AND CONFIDENTIAL THE INFORMATION CONTAINED IN THIS DRAWING IS THE SOLE PROPERTY OF UNIVERSITY OF TEXAS AT ARLINGTON. ANY REPRODUCTION IN PART OR AS A WHOLE WITHOUT THE WRITTEN PERMISSION OF THE DEPARTMENT OF BIOENGINEERING IS PROHIBITED.	UNLESS OTHERWISE SPECIFIED **DIMENSIONS ARE IN CENTIMETERS** **TOLERANCES:** TWO PLACE DECIMAL ± .05 THREE PLACE DECIMAL ± .025	**DRAWN BY:** P.Zengxing **Date:** 8/05/2018 **MATERIAL:** SLA RESIN	**TITLE:** TOP INTERNAL SHEATH **FILE NAME:** PROBE_SHEATH_2.SLDPRT **SCALE:** 2 : 1	**REV. NO.** 5